AIAA AVIATION Forum
12-16 June 2023, San Diego, CA and Online
AIAA AVIATION 2023 Forum

10.2514/6.2023-3652

# Cyclostationary analysis of forced turbulent jets

Liam Heidt * and Tim Colonius †
*California Institute of Technology, Pasadena, CA USA*

Akhil Nekkanti ‡ and Oliver T. Schmidt§
*University of California San Diego, La Jolla, CA USA*

Igor A. Maia¶ and Peter Jordan‖
*Institut Pprime-CNRS-Université de Poitiers-ENSMA, Poitiers France*

**A variety of actuation methods have been applied to turbulent jets with the aim of reducing far-field sound. However, a detailed understanding of the mechanisms by which actuation alters the turbulence and far-field sound is lacking. We investigate the effect of periodic acoustic forcing by performing a series of large-eddy simulations of turbulent axisymmetric subsonic and supersonic jets subjected to periodic forcing at several frequencies and amplitudes. To analyze data from the forced jets, we employ cyclostationary analysis, which is an extension of the statistically stationary framework to processes that have periodically varying statistics. Both low-** $St_f = 0.3$ **and high-frequency** $St_f = 1.5$ **forcing generate an energetic tonal response but have limited effect on the time-averaged mean with a forcing amplitude greater than 1% required to achieve a small change. Similar trends were seen for the turbulent kinetic energy and the energy transfer between the mean and turbulent components. By applying cyclostationary spectral proper orthogonal decomposition (CS-SPOD), we investigate how the dominant coherent structures are modified and modulated by the forcing. For** $St_f = 0.3$**, a broadband increase in the energy of the dominant coherent structures was found. The low-frequency coherent structures were found to be strongly phase dependent, with substantial energy coupled to the high-velocity and high-shear regions of the mean flow. In contrast, forcing at** $St_f = 1.5$ **resulted in a broadband decrease in the energy of the dominant coherent structures. No phase-dependent modulation of the low-frequency coherent structures was seen due to a large difference in the wavelength and spatial support between the coherent structures and the mean field. A reduced impact of the** $St_f = 0.3$ **forcing on the supersonic jet is seen, while the** $St_f = 1.5$ **forcing results in a similar impact.**



## I. Introduction

Reducing the jet noise produced by tactical aircraft is difficult due to the low-bypass-ratio engines required by these aircraft. Thus, employing the successfully utilized commercial aviation approach of increasing the bypass ratio is not possible. Instead, several methods have been developed to subtly alter the flow. Both passive (chevrons, tabs, etc.) and active (fluidic injection, plasma actuators, etc.) control devices have been employed to successfully reduce peak aft-angle radiation by up to 5dB [1]. Of particular interest are active control devices as they avoid potential performance losses in portions of the flight envelope where noise mitigation is not of primary concern. However, these control devices are empirically designed and we typically lack a mechanistic understanding that would enable them to be scaled and improved.

Amongst studies seeking to characterize mechanisms, Kœnig et al. [2] studied the effect of unsteady forcing on the noise produced by a subsonic turbulent jet. Two forcing frequencies $St_f = 0.23,\ 0.46$ at an azimuthal mode

*PhD Candidate, Graduate Aerospace Laboratories of the California Institute of Technology, AIAA Student Member
†Frank and Ora Lee Marble Professor of Mechanical Engineering, Mechanical and Civil Engineering, Associate Fellow AIAA
‡PhD Student, Department of Mechanical and Aerospace Engineering, AIAA Student Member
§Assistant Professor, Department of Mechanical and Aerospace Engineering, Senior Member AIAA.
¶Post-Doctoral Research Fellow, Département of Fluides Thermique et Combustion, Institut Pprime-CNRS-Université de Poitiers-ENSMA, Poitiers France.
‖Directeur de Recherche, Département of Fluides Thermique et Combustion, Institut Pprime-CNRS-Université de Poitiers-ENSMA, Poitiers France.

number $m = 2$ were studied. They found that the lower forcing frequency resulted in a broadband increase in noise production which, by using the parabolized stability equations, they linked to the turbulent mean flow strongly amplifying disturbances at the lower forcing frequency (and azimuthal mode number). Consequently, the lower frequency forcing produced, in addition to a modification of the mean, a strong tonal response that led to a considerable increase in the noise. In contrast, the high-frequency forcing resulted in a broadband noise reduction which was linked to the forcing deforming the mean flow to one that was more stable. Similarly, Sinha et al. [3] investigated the effect of steady and periodic mass injection on the noise produced by a Mach 1.5 supersonic axisymmetric jet. They showed that jet noise reduction was uniquely linked to the steady component of the forcing applied. Applying unsteady forcing in addition to the steady component resulted in the creation of highly energetic tones at the forcing frequency and its harmonics which overwhelmed the broadband noise reduction created by the steady forcing. These experimental studies suggest that jet noise reduction does not result from any direct interaction between the forcing and the background turbulence. Instead, it is a by-product of Reynolds stresses that are generated by the tonal disturbances (which are independent from those of the background turbulence) that deform the turbulent mean flow of the jet and thus alter the entire turbulence spectrum.

A fundamental assumption frequently evoked to study natural jets is statistical stationarity, meaning that the statistical characteristics of the system are invariant in time. This is a valid assumption for unforced jets; however, in cases where forcing is applied, this fundamental assumption breaks down as the flow, and thus statistics, are expected to be correlated to the forcing. Thus, to analyze the full impact of the forcing on the flow, one must depart from the statistically stationary framework. Flows where the statistics vary periodically, as is expected in a turbulent jet when subjected to a harmonic forcing, can be studied using cyclostationary analysis. Cyclostationary analysis, popularized and heavily developed by Hurd [4], Gardner [5], among many others [6–9], is an extension of statistically stationary analysis to processes with periodically varying statistics. While it is well known and employed in the signal processing and mechanics community, it is relatively unknown to the turbulence/fluid dynamics community. All commonly used statistically stationary descriptors (cross-correlation, cross-spectral density, etc) have equivalent cyclostationary forms that collapse back to their stationary counterpart when analyzing stationary flows, making it ideal for studying these processes.

Among the myriad of tools used to study turbulent jets, spectral proper orthogonal decomposition (SPOD) [10–12] has recently been employed successfully to study the instability mechanisms present in natural (unforced) turbulence jets, see for example [13–18]. By determining the energy spectra and decomposing the flow into energy-ranked coherent structures, these studies could identify and analyze the mechanisms, such as the Kelvin-Helmholtz, Orr, and lift-up, present. Recent studies [19] have investigated a forced turbulent jet while naively assuming a statistically stationary assumption. However, since SPOD requires a statistically stationary assumption, this is not valid for forced turbulent jets. To study turbulent flows that exhibit periodic statistics, Heidt and Colonius [20] recently developed cyclostationary SPOD (CS-SPOD) through an extension to Kim et al. [21], which extends SPOD to the case with cyclostationary statistics. CS-SPOD shares similar properties to SPOD and naturally collapses back to SPOD when analyzing a statistically stationary process making it ideal for studying forced turbulent flows.

To study forced turbulent jets, we perform a series of high-fidelity large-eddy simulations of turbulent subsonic and supersonic jets subjected to a periodic acoustic forcing. We first study the subsonic jet and investigate the impact of the forcing on the mean flow and how the turbulence present in the jet is correlated to (i.e. modulated by) the applied forcing. Next, we investigate the energy transfer between the applied forcing and turbulence via a cyclostationary decomposition of the Navier-Stokes equation. We then study the impact of the forcing on the coherent structures present in the flow through CS-SPOD. Lastly, we then conduct an analogous study on a similar supersonic jet.

## II. Cyclostationary analysis and CS-SPOD

In this section, we briefly introduce the theory of cyclostationary analysis. A cyclostationary process is one where the statistics of the process vary periodically in time, and for a full review we refer the reader to Gardner [7], Gardner et al. [22], Napolitano [23]. Let $\boldsymbol{q}(\boldsymbol{x}, t)$ be a possibly complex-valued process at time $t$ over the set of independent variables $\boldsymbol{x}$. The process $\boldsymbol{q}(\boldsymbol{x}, t)$ can be split into its first- and second-order components. The first order component $E\{\boldsymbol{q}(\boldsymbol{x}, t)\}$ of $\boldsymbol{q}(\boldsymbol{x}, t)$ is periodic with period $T_0$, i.e. $E\{\boldsymbol{q}(\boldsymbol{x}, t)\} = E\{\boldsymbol{q}(\boldsymbol{x}, t + T_0)\}$, and is defined as the expectation of the process over a number of realizations, where $E\{\cdot\}$ is the expectation operator. The second order component, also known as the residual/turbulent component, is then defined as the difference between the original process and the first order component

$$\boldsymbol{q}''(\boldsymbol{x}, t) \equiv \boldsymbol{q}(\boldsymbol{x}, t) - E\{\boldsymbol{q}(\boldsymbol{x}, t)\}. \tag{1}$$

Antoni et al. [24] and Antoni [25] demonstrated that in physical systems, it is crucial to analyze the first- and second-order components separately. This is because the first-order component is the deterministic tonal component that originates

from the forcing, while the second-order component is the stochastic (turbulent) component that is modulated by the forcing. This is similar to the triple decomposition [26, 27] where the underlying flow is separated into the first-order (phase-averaged) and second-order (turbulent/residual) components. Assuming cycloergodicity, the expectation can be replaced by the phase average

$$\widetilde{\boldsymbol{q}}(\boldsymbol{x},t) = E\{\boldsymbol{q}(\boldsymbol{x},t)\} = \lim_{K\to\infty}\frac{1}{K}\sum_{k=0}^{K}\boldsymbol{q}(\boldsymbol{x},t+kT_0). \tag{2}$$

Thus, for the remainder of this section, we assume that the process $\boldsymbol{q}(\boldsymbol{x},t)$ is a zero-mean process (or has had its mean removed).

The cross-correlation function of a process quantifies the dependence between two processes at two different points in time and is defined as

$$\boldsymbol{C}(\boldsymbol{x},\boldsymbol{x}',t,\tau) \equiv E\{\boldsymbol{q}(\boldsymbol{x},t+\tau/2)\boldsymbol{q}^*(\boldsymbol{x}',t-\tau/2)\}, \tag{3}$$

where $\tau$ represents the difference in time. For a cyclostationary process, the cross-correlation function is periodic in time, meaning that it can be expressed as the following Fourier series

$$\boldsymbol{C}(\boldsymbol{x},\boldsymbol{x}',t,\tau) \equiv \boldsymbol{C}(\boldsymbol{x},\boldsymbol{x}',t+T_0,\tau), \tag{4a}$$

$$= \sum_{k=-\infty}^{\infty}\hat{\boldsymbol{C}}_{k\alpha_0}(\boldsymbol{x},\boldsymbol{x}',\tau)e^{i2\pi k\alpha_0 t}, \tag{4b}$$

where $T_0$ is the period, $\alpha_0$ is the fundamental periodicity frequency present in the system (typically the forcing frequency), $\alpha = k\alpha_0$ is the cycle frequency that represents how the statistics are modulated in time, and $(\cdot)^*$ is the Hermitian transpose. The Fourier series coefficients $\hat{\boldsymbol{C}}_{k\alpha_0}(\boldsymbol{x},\boldsymbol{x}',\tau)$ are known as the cyclic cross-correlation functions at cycle frequency $k\alpha_0$ and represent how the cross-correlation function varies as a function of time. The cyclostationary equivalent of the CSD tensor is the cyclic cross-spectral density (CCSD) tensor. The CCSD is the Fourier transform of the cyclic cross-correlation function and is written as

$$\boldsymbol{S}_{k\alpha_0}(\boldsymbol{x},\boldsymbol{x}',f) = \int_{-\infty}^{\infty}\hat{\boldsymbol{C}}_{k\alpha_0}(\boldsymbol{x},\boldsymbol{x}',\tau)e^{-i2\pi f\tau}d\tau, \tag{5}$$

where $f$ is the spectral frequency. We note that the standard cross-spectral density (CSD) tensor is the $0^{th}$ Fourier series component of the CCSD, $\boldsymbol{S}_0(\boldsymbol{x},\boldsymbol{x}',f)$. Combining Eqs. 5 and 4b, and then taking the inverse Fourier series with respect to the cycle frequencies gives the Wigner-Ville spectrum [28–30]

$$\boldsymbol{WV}(\boldsymbol{x},\boldsymbol{x}',t,f) = \sum_{k=-\infty}^{\infty}\boldsymbol{S}_{k\alpha_0}(\boldsymbol{x},\boldsymbol{x}',f)e^{i2\pi k\alpha_0 t}. \tag{6}$$

The Wigner-Ville spectrum is a time-frequency representation of how the correlation between $\boldsymbol{q}(\boldsymbol{x},t)$ and $\boldsymbol{q}(\boldsymbol{x}',t)$ at spectral frequency $f$ varies over time (or equivalently as a function of the forcing phase). When $\boldsymbol{x}$ and $\boldsymbol{x}'$ are equal, then the Wigner-Ville spectrum describes how the power-spectral density (PSD) varies as a function of phase.

To estimate the CCSD in practice, after assuming cycloergodicity, we employ Welch's method [31] as employed in Heidt and Colonius [20], Antoni [30], which we refer readers to for details. The Wigner-Ville spectrum is then computed using the estimates of the CCSD but is limited to $k_{max}$ harmonics of the forcing frequency, i.e. $\boldsymbol{WV}(\boldsymbol{x},\boldsymbol{x}',t,f) = \sum_{k=-k_{max}}^{k_{max}}\boldsymbol{S}_{k\alpha_0}(\boldsymbol{x},\boldsymbol{x}',f)e^{i2\pi k\alpha_0 t}$.

In order to study the coherent structures present in harmonically forced turbulent flows, Heidt and Colonius [20] developed CS-SPOD, which is the cyclostationary extension of regular SPOD. Like SPOD, CS-SPOD seeks to determine modes $\boldsymbol{\phi}(\boldsymbol{x},t)$ that optimally reconstruct the second-order statistics of the flow. However, because the flow is cyclostationary, frequency-by-frequency analysis, as performed in SPOD, is no longer possible. Instead, the eigenvectors are assumed to contain spectral components at $\Omega_\gamma = \{\cdots,\ \gamma-2\alpha_0,\ \gamma-\alpha_0,\ \gamma,\ \gamma+\alpha_0,\ \gamma+2\alpha_0,\ \cdots\}$ and have the following periodic time-domain form $\boldsymbol{\phi}(\boldsymbol{x},t) = \sum_{m=-\infty}^{\infty}\boldsymbol{\psi}(\boldsymbol{x},\gamma+m\alpha_0)e^{i2\pi(\gamma+m\alpha_0)t}$. This gives them a periodic amplitude/energy and allows them to capture the time-periodic statistics of the flow. The final eigenvalue problem can be compactly written as

$$\int_\Omega \boldsymbol{S}(\boldsymbol{x},\boldsymbol{x}',\gamma)\boldsymbol{W}(\boldsymbol{x}')\boldsymbol{\Psi}(\boldsymbol{x}',\gamma)\mathrm{d}\boldsymbol{x}' = \lambda\boldsymbol{\Psi}(\boldsymbol{x},\gamma), \tag{7}$$

where

$$\boldsymbol{S}(\boldsymbol{x},\boldsymbol{x}',\gamma) = \tag{8a}$$
$$\begin{bmatrix} \ddots & \ddots & \ddots & \ddots & \ddots \\ \ddots & \boldsymbol{S}_0(\boldsymbol{x},\boldsymbol{x}',\gamma-\alpha_0) & \boldsymbol{S}_{-\alpha_0}(\boldsymbol{x},\boldsymbol{x}',\gamma-\frac{\alpha_0}{2}) & \boldsymbol{S}_{-2\alpha_0}(\boldsymbol{x},\boldsymbol{x}',\gamma) & \ddots \\ \ddots & \boldsymbol{S}_{\alpha_0}(\boldsymbol{x},\boldsymbol{x}',\gamma-\frac{\alpha_0}{2}) & \boldsymbol{S}_0(\boldsymbol{x},\boldsymbol{x}',\gamma) & \boldsymbol{S}_{-\alpha_0}(\boldsymbol{x},\boldsymbol{x}',\gamma+\frac{\alpha_0}{2}) & \ddots \\ \ddots & \boldsymbol{S}_{2\alpha_0}(\boldsymbol{x},\boldsymbol{x}',\gamma) & \boldsymbol{S}_{\alpha_0}(\boldsymbol{x},\boldsymbol{x}',\gamma+\frac{\alpha_0}{2}) & \boldsymbol{S}_0(\boldsymbol{x},\boldsymbol{x}',\gamma+\alpha) & \ddots \\ \ddots & \ddots & \ddots & \ddots & \ddots \end{bmatrix},$$

$$\boldsymbol{W}(\boldsymbol{x}) = \begin{bmatrix} \ddots & & & & \\ & \boldsymbol{W}(\boldsymbol{x}) & & & \\ & & \boldsymbol{W}(\boldsymbol{x}) & & \\ & & & \boldsymbol{W}(\boldsymbol{x}) & \\ & & & & \ddots \end{bmatrix}, \tag{8b}$$

$$\boldsymbol{\Psi}(\boldsymbol{x},\gamma) = \begin{bmatrix} \vdots \\ \boldsymbol{\psi}(\boldsymbol{x},\gamma-\alpha_0) \\ \boldsymbol{\psi}(\boldsymbol{x},\gamma) \\ \boldsymbol{\psi}(\boldsymbol{x},\gamma+\alpha_0) \\ \vdots \end{bmatrix}. \tag{8c}$$

$\boldsymbol{S}(\boldsymbol{x},\boldsymbol{x}',\gamma)$ is the CS-SPOD decomposition tensor, $\boldsymbol{W}(\boldsymbol{x})$ is the concatenated weight tensor, and $\boldsymbol{\Psi}(\boldsymbol{x},\gamma)$ are the CS-SPOD eigenvectors. The time-domain version of the CS-SPOD eigenvectors $\boldsymbol{\phi}(\boldsymbol{x},t)$ have Fourier series coefficients, at each $f \in \Omega_\gamma$, of $\boldsymbol{\psi}(\boldsymbol{x},f)$. This coupling of frequencies in CS-SPOD occurs because frequency components separated by $n\alpha_0$ are correlated to each other, meaning that each frequency component can not be solved individually. In contrast, stationary processes do not exhibit correlation between frequencies, and thus each frequency can be solved independently via SPOD. Due to this coupling, CS-SPOD performed at $f$ and $f+\alpha_0$ solve the same problem, i.e. giving $\Omega_\gamma = \Omega_{\gamma+z\alpha_0}$, where $z \in \mathbb{Z}$, meaning that CS-SPOD only contains unique solutions for the frequency sets corresponding to $\gamma = (-\alpha_0/2,\ \alpha_0/2]$. This decomposition results in a countably infinite set of eigenfunctions $\boldsymbol{\Psi}_j(\boldsymbol{x},\gamma)$ at $\gamma$ that are orthogonal to all other modes at the same $\gamma$ in the spatial inner norm $\langle \boldsymbol{q}_1,\boldsymbol{q}_2\rangle_x = \int_\Omega \boldsymbol{q}_2^*(\boldsymbol{x},t)\boldsymbol{W}(\boldsymbol{x})\boldsymbol{q}_1(\boldsymbol{x},t)\mathrm{d}\boldsymbol{x}$, i.e. $\langle \boldsymbol{\Psi}_j(\boldsymbol{x},\gamma),\boldsymbol{\Psi}_k(\boldsymbol{x},\gamma)\rangle_x = \delta_{j,k}$ and are optimal in terms of the amount of energy they capture. In this work, we employ the Chu-compressible energy norm [32] that has been applied in previous SPOD studies [33], which maximizes the kinetic, thermal, and potential energy.

Since the infinite problem can not be solved numerically, $\Omega_\gamma$ is limited to $a_1$ number of harmonics such that $\Omega_\gamma = \{-a_1\alpha_0+\gamma,\ (-a_1+1)\alpha_0+\gamma,\ \cdots,\gamma,\ \cdots,(a_1-1)\alpha_0+\gamma,\ a_1\alpha_0+\gamma\}$. $a_1$ should be chosen such that $\Omega_\gamma$ encompasses all frequencies of interest and sufficient energy. Heidt and Colonius [20] also proposed an efficient computational procedure to compute CS-SPOD. They employed the Welch spectral density estimation technique in conjunction with the method of snapshots technique [34] and a frequency-shifting technique to substantially reduce the computational cost (and memory) of computing CS-SPOD to a level similar to standard SPOD.

## III. Cyclostationary compressible Navier-Stokes equations

To determine how the forcing interacts with the turbulence, we perform a cyclostationary decomposition of the governing equations. In particular, we wish to determine how the turbulence is modulated by (interacts with) the forcing and to what degree there is energy transfer between the mean flow field and the turbulent field.

Since we are studying a compressible flow, we will perform a Favre-averaging of the governing equations. Let $f(x,t)$ be a real-valued cyclostationary process and let $\rho(x,t)$ represent the density. We employ two averages, the ensemble average $\overline{f}(x,t) = \langle f(x,t)\rangle$ and the density-weighted (Favre) ensemble average $\widetilde{f}(x,t) = \{f(x,t)\} = \langle\rho(x,t)f(x,t)\rangle/\langle\rho(x,t)\rangle$. Assuming cycloergodicity, these averages can be computed using the phase average (as shown in Eq. 2) instead of the expectation operator. These averages, for a cyclostationary process, become periodic functions in time and naturally become the long-time average for a statistically-stationary process. We denote the $0^{th}$ frequency component of the mean as the period-average since the long-time average does not converge for a periodic function. As demonstrated in Eq. (1), we can now decompose a process into its first-order $\overline{f}(x,t)$, $\widetilde{f}(x,t)$ and second-order $f'(x,t)$,

$f''(x,t)$ components with reference to the ensemble and Favre-ensemble averages, respectively, such that

$$f(x,t) = \overline{f}(x,t) + f'(x,t), \tag{9a}$$
$$f(x,t) = \widetilde{f}(x,t) + f''(x,t), \tag{9b}$$

noting that, $\overline{f'} = 0$, $\overline{\rho f''} = 0$, and $\overline{f''} \neq 0$. We decompose the compressible Navier-Stokes equations in a manner similar to Huang et al. [35]. The relevant variables are decomposed as follows

$$\rho' = \rho - \overline{\rho}, \tag{10a}$$
$$u_i'' = u_i - \widetilde{u}_i, \tag{10b}$$
$$T'' = T - \widetilde{T}, \tag{10c}$$
$$\overline{p} = \overline{\rho} R \widetilde{T} = \overline{\rho} R (\overline{T} - \overline{T''}), \tag{10d}$$
$$p' = \rho' R \widetilde{T} + \overline{\rho} R T'' + \rho' R T'', \tag{10e}$$
$$\widetilde{u_i'' u_j''} = \{u_i'' u_j''\} = \overline{\rho u_i'' u_j''}/\overline{\rho}, \tag{10f}$$

where we have omitted the explicit spatial and temporal dependence for clarity and $u_i$ is the velocity in the $i, j, k$ directions, $T$ is the temperature, $R$ is the gas constant, and the ideal gas assumption has been made. The derivation of the governing equations presented in Huang et al. [35] is invariant to the type of ensemble average (i.e, applied to statistically stationary or cyclostationary flows), thus, we obtain similar equations and refer the reader to Huang et al. [35] for a detailed discussion. Critically, the energy transfer between the mean and turbulent component is given by

$$\widetilde{E} = -\overline{\rho} \widetilde{u_i'' u_j''} \frac{\partial \widetilde{u}_i}{\partial x_j}, \tag{11}$$

and is a source in the turbulent kinetic energy equation and a sink in the mean kinetic energy equation. Unlike the Reynolds/triple decomposition [26, 36], we obtain a phase-dependent energy transfer that allows us to investigate how the energy transfer between the mean field and turbulent field varies as a function of phase.

## IV. Large-eddy simulations of turbulent jets

Large-eddy simulations of isothermal and perfectly expanded Mach 0.4 and Mach 1.5 forced jets are performed using the compressible flow solver "Charles" by Cascade Technologies [37, 38]. Charles solves the spatially filtered compressible Navier–Stokes equations on unstructured grids using a density-based finite-volume method. Computations performed on an unforced Mach 0.9 turbulent jet have shown excellent agreement between the computational and experimental mean, first-order statistics, and sub-decibel agreement between the computational and experimental noise spectra [38] at all relevant angles and frequencies.

As in previous computations [38], the jet nozzle is explicitly included in the computational domain, and synthetic turbulence is applied inside the nozzle to obtain a fully turbulent boundary layer. The reader can find details on the numerical methods, subgrid-models, and meshing in Brès et al. [37]. To account for the forcing, a slightly refined grid is employed compared to the natural jet simulations investigated previously [37, 38], and a total of 19.2 and 42.7 million control volumes are employed for the subsonic and supersonic jets, respectively. A representative schematic of the simulation set up is shown in Fig. 1. The subsonic and supersonic jets have a Reynolds number, $Re_j = \rho_j U_j D/\mu_j = 4.5 \times 10^5, 1.76 \times 10^6$, respectively, and both jets have a Prandtl number of 0.7. The subscripts j and $\infty$ represent the jet and free-stream conditions, respectively. $\rho$ is the density, $\mu$ is the viscosity, $M_j = U_j/c_j$ is the Mach number where $c_j$ and $U_j$ are the speed of sound, and natural jet mean flow velocity magnitude, respectively. Throughout this paper, the flow is non-dimensionalized by the jet exit values, lengths by the jet diameter $D$, and pressure by $\rho_j U_j^2$. Frequencies are expressed with respect to the Strouhal number $St = fD/U_j$, where $f$ is the frequency. For numerical stability, the simulations contain a weak $M_\infty = 0.009, 0.1$ coflow for the subsonic and supersonic jets, respectively.

The forcing is applied as planar acoustic waves in an annular region around the nozzle with a non-dimensional frequency $St_f = f_f D/U_j$ and amplitude $a_0$, where $f_f$ is the forcing frequency. The magnitude of the acoustic forcing applied along the co-flow boundary is scaled by the function $c(r)$, which results in the acoustic forcing decaying in an error-function manner about $r = 5$. Nekkanti [39] validated a similar forcing strategy for a similar turbulent jet against the experimental data by Maia [40–42], showing excellent agreement. Along with the natural unforced jet, simulations are run at $St_f = 0.3,\ 1.5$ $(a_0/U_j = 1\%, 10\%)$ for the subsonic jet and $St_f = 0.3,\ 1.5$ $(a_0/U_j = 1\%)$ for

the supersonic jet. A forcing frequency of $St_f = 0.3$ was chosen to roughly match the forced jet experiments of Crow and Champagne [43], where $St_f = 0.3$ was observed as the frequency that led to the largest amplification by the flow (i.e. the *jet preferred mode*). The $St_f = 1.5$ case was chosen as experimental studies [44, 45] have shown a broadband reduction in jet noise for both subsonic and supersonic jets at this frequency. The acoustic forcing is defined by the following relations:

$$
\begin{aligned}
c(r) &= 0.5\left[1 - \mathrm{erf}\left(2(r-5)\right)\right], \\
u_f(r,t) &= c(r)\sin(2\pi f_f t), \\
u_x(r,t) &= u_\infty + a_0 u_f(r,t), \\
u_r(r,t) &= u_\theta(r,t) = 0, \\
\rho(r,t) &= \rho_\infty + \rho_\infty(u_x(r,t) - u_\infty)/a_\infty, \\
p(r,t) &= p_\infty + a_\infty \rho_\infty (u_x(r,t) - u_\infty).
\end{aligned}
$$

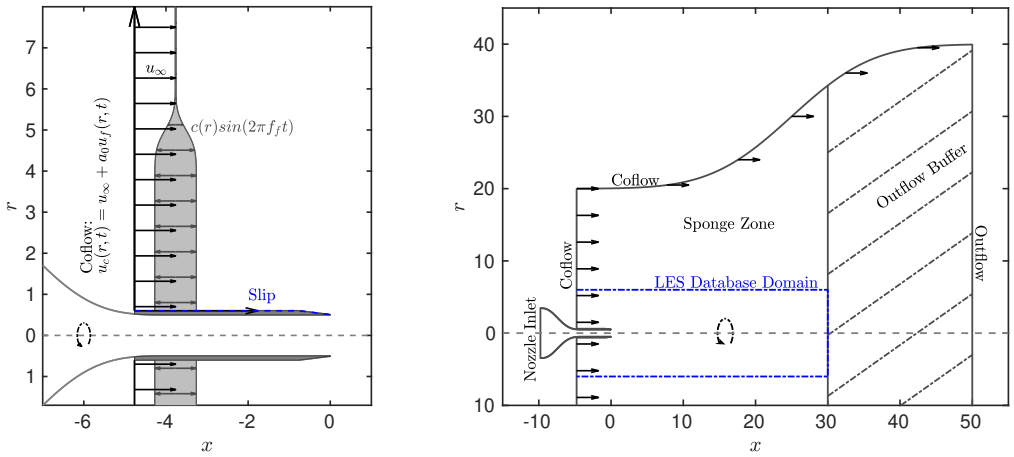


**(a) Nozzle region schematic** **(b) Full domain schematic**

**Fig. 1 LES simulation schematic, adapted from Brès et al. [38].**

The simulations are run with a computational time step $\Delta t D/c_\infty = 0.001, 0.000225$ and a total simulation time $t_{sim} D/c_\infty = 4000, 1000$ (after the initial transient, due to the forcing, has passed), for the subsonic and supersonic jets respectively. The unstructured LES data for the subsonic and supersonic jets were interpolated onto structured cylindrical grids that mimics the LES resolution of ($n_x \times n_r \times n_\theta = 656 \times 138 \times 128,\ 698 \times 136 \times 128$), respectively. The forced cases were saved at $N_{\theta_f}$ phases per forcing oscillation resulting in a temporal spacing between snapshots of $\frac{\Delta t c_\infty}{D}$. A summary of the simulations performed is shown in Table 1, and an instantaneous snapshot of the natural and forced subsonic and supersonic jets is shown in Fig. 2.

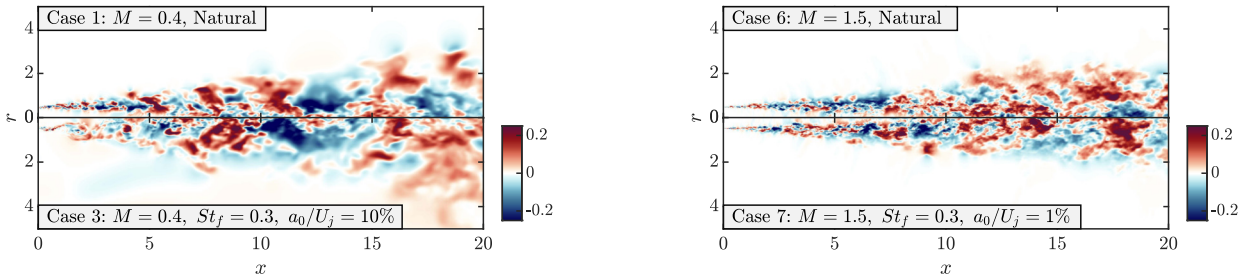


**(a) Mach 0.4** **(b) Mach 1.5**

**Fig. 2 Instantaneous snapshot of $u_x''$ for the Mach 0.4 and Mach 1.5 turbulent jets.**

| Case | $M_j$ | $St_f$ | $a_0/U_j$ | $\frac{\Delta t c_\infty}{D}$ | $N_{\theta_f}$ |
|---|---|---|---|---|---|
| Case 1: $M = 0.4$, Natural | 0.4 | — | — | 0.2 | — |
| Case 2: $M = 0.4,\ St_f = 0.3,\ a_0/U_j = 0.01$ | 0.4 | 0.3 | 0.01 | 0.174 | 48 |
| Case 3: $M = 0.4,\ St_f = 0.3,\ a_0/U_j = 0.1$ | 0.4 | 0.3 | 0.1 | 0.174 | 48 |
| Case 4: $M = 0.4,\ St_f = 1.5,\ a_0/U_j = 0.01$ | 0.4 | 1.5 | 0.01 | 0.138 | 12 |
| Case 5: $M = 0.4,\ St_f = 1.5,\ a_0/U_j = 0.1$ | 0.4 | 1.5 | 0.1 | 0.138 | 12 |
| Case 6: $M = 1.5$, Natural | 1.5 | — | — | 0.045 | — |
| Case 7: $M = 1.5,\ St_f = 0.3,\ a_0/U_j = 0.01$ | 1.5 | 0.3 | 0.01 | 0.0463 | 48 |
| Case 8: $M = 1.5,\ St_f = 1.5,\ a_0/U_j = 0.01$ | 1.5 | 1.5 | 0.01 | 0.0371 | 12 |

**Table 1 Parameters of the simulations performed.**



# V. Subsonic jet

## A. Mean flow

We begin with an analysis of the impact of the forcing on the mean flow. It is known that high-Reynolds number turbulent jets are receptive to a wide range of forcing frequencies and azimuthal mode numbers, for example, [3, 43–45]. Generally, forcing results in a shorter jet as well as a thickening of the shear layer, which can be seen in Figs. 3 - 4.

In Fig. 3a, we display the mean axial velocity for the subsonic jets corresponding to a forcing phase $\theta_f = 0°$. For the $St_f = 0.3$ forcing, a large modulation of the mean is observed with the largest impact along the potential core region. As the forcing amplitude increases, we clearly observe a greater impact on the mean field with regions of increasingly low and high axial velocity resulting in vortex roll-up as seen in Fig. 2a. In contrast, the $St_f = 1.5$ has a more compact spatial impact upon the mean and is spatially limited to the near-nozzle region. Due to the large amplitude of forcing applied, the $St_f = 1.5, a_0/U_j = 10\%$ acoustic waves have steepened as they propagate downstream and are beginning to exhibit shock-like structures resulting in the kinking of the mean velocity profile. In Fig. 3b, we display the $0^{th}$ frequency component of the phase average (i.e. the period-average). Despite the jet's strong harmonic response to the forcing, we see that the impact on the period-averaged field is minor, with just a small reduction in the length of the 25% contour line across all cases.

In Fig. 4, we display the period-averaged axial velocity $\overline{u}_{x,0}(x)$ and the standard deviation of the mean velocity $\sigma(\overline{u}_x(x))$ along the centerline and lipline, and the momentum thickness $\delta_\theta$. Similar to previous studies [33], $\delta_\theta$ is defined as

$$\delta_\theta(x) = \int_0^{r_{0.05}} \frac{\overline{\rho}_0(x,r)\overline{u}_{x,0}(x,r)}{\overline{\rho}_0(x,0)\overline{u}_{x,0}(x,0)} \left(1 - \frac{\overline{u}_{x,0}(x,r)}{\overline{u}_{x,0}(x,0)}\right) \mathrm{d}r,$$

where $\overline{u}_{x,0}(x,r)$ is the time- and azimuthally averaged streamwise velocity. The radial bound on the integral, $r_{0.05}$, corresponds to the radial location where $\overline{u}_{x,0}(x,r_{0.05}) - U_\infty = 0.05\ \overline{u}_{x,0}(x,0)$. As seen in Fig. 3a, for all forcing frequencies and amplitudes, the jet becomes shorter as it spreads more rapidly, as seen through a decrease in the centerline velocity and an increase in the momentum thickness. We also see that the $St_f = 0.3$ forcing has a substantially greater and more global impact on the mean field than the $St_f = 1.5$ forcing. The $St_f = 0.3$ forcing results in large modulations of the centerline and lipline velocities from the nozzle exit until $\approx 8$ diameters downstream, after which the effect of the forcing rapidly decreases. We see that the $St_f = 0.3,\ a_0/U_j = 10\%$ forcing, due to the high amplitude employed and the resulting strong nonlinear interactions, results in a non-monotonically decreasing period-averaged centerline velocity in contrast to all other cases. The modulation of the mean is also increasingly affected, with a maximum standard deviation (as a ratio of the jet velocity) along the centerline of 15%, 33% and along the lipline of 9.8%, 35% for the $a_0/U_j = 1\%$ and $a_0/U_j = 10\%$ forcing, respectively. In contrast, the $St_f = 1.5$ forcing is more localized to the near-nozzle exit, with the only substantial modulation of the lipline velocity profile occurring within the first 0.15 diameters downstream from the nozzle exit with a standard deviation of 7.0%, 18% for the $a_0/U_j = 1\%$ and $a_0/U_j = 10\%$ forcing, respectively. The effect of the $St_f = 1.5$ forcing along the centerline is minimal, with a maximum modulation of just 3.5% for the $a_0/U_j = 10\%$ forcing, demonstrating the localized receptivity of the forcing. Overall, both frequencies and amplitudes result in a substantial modulation of the mean as a function of phase, but the impact on the period-averaged values is minor, consistent with the trends seen in the literature.

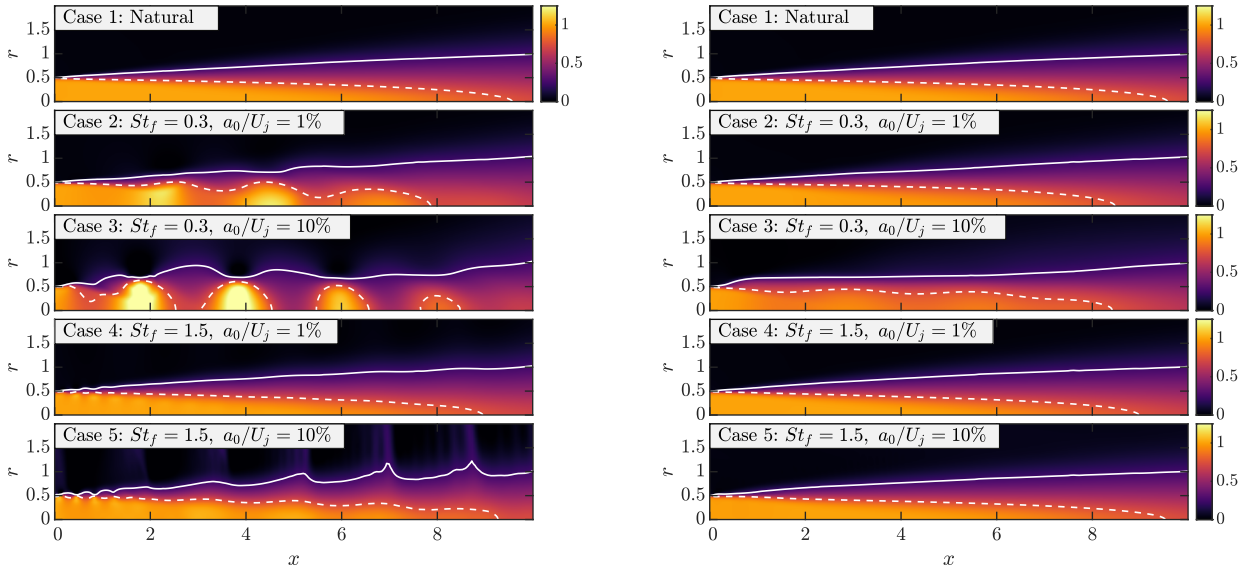


**Fig. 3 Contours of the mean (phase-averaged) axial velocity $\overline{u}_x$ at $\theta_f = 0$ (a) and the $f = 0$ component (period-averaged component) of the axial velocity $\overline{u}_{x,0}$ (b) for the subsonic jet. The solid and dashed white lines correspond to contours of $\overline{u}_x = 0.25, 0.75$ and $\overline{u}_{x,0} = 0.25, 0.75$ for (a) and (b), respectively.**

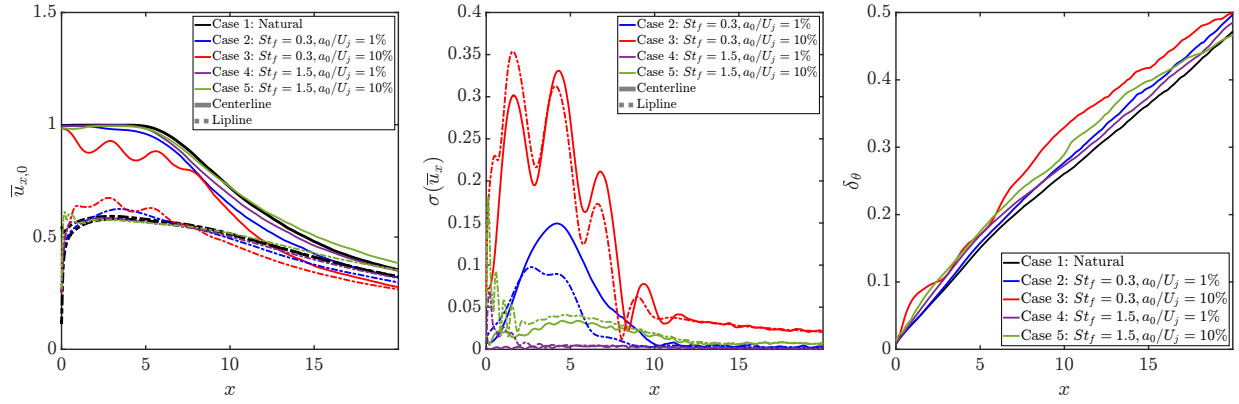


**Fig. 4 Period-averaged axial velocity $\overline{u}_{x,0}$ (a) and standard-deviation of the mean axial velocity $\sigma(\overline{u}_x)$ (b) along the centerline and lipline, and momentum thickness $\delta_\theta$ (c) of the subsonic jet.**

### B. Second-order statistics

In Fig. 5a, we display contours of the azimuthally averaged root-mean-square (RMS) of the axial velocity $\{u_x'' u_x''\}$ at $\theta_f = 0$. The $St_f = 0.3$ forcing results in a modulation of the RMS that has a maximum at the end of the potential core, which corresponds to the maximum modulation of the mean. The effect for $St_f = 0.3,\ a_0/U_j = 1\%$ is mild, whereas for $St_f = 0.3,\ a_0/U_j = 10\%$, a large amount of turbulence is present within the advecting vortices. Similar to the mean field, the effect of the $St_f = 1.5$ forcing is limited to the near-nozzle region with no strong phase-dependency observed after around 2 diameters downstream for both forcing amplitudes.

In Fig. 5b, we plot the period-averaged axial velocity RMS along the centerline and lipline. We see that both $St_f = 0.3$ forcings result in a minor upstream shift of the centerline RMS which is expected given the minor shortening of the jet previously observed. Additionally, an increase in the peak centerline and lipline RMS is observed, indicating that the period-averaged intensity of the turbulence has been increased. A more substantial effect on the lipline RMS is

seen, with a large decrease in the RMS for the first 4 diameters and then a substantial increase between $x \in [6, 11]$ diameters downstream. This decrease in the period-averaged RMS is due to the mean field (and thus the shear layer) being modulated towards and away from the centerline as a function of the phase of the forcing, thereby resulting in a lower period-averaged value. The substantial increase in the RMS at $x \in [5, 11]$ is likely caused by the highly energetic vortices generated by the forcing. These vortices advect downstream while breaking down, thereby creating a substantial amount of turbulent energy. For the $St_f = 1.5,\ a_0/U_j = 10\%$ forcing, the RMS contours clearly show the presence of vortex roll-up. However, in contrast to the $St_f = 0.3$ case, these vortices are smaller in size and are spatially restricted to $x \in [0, 2]$. Subsequently, these vortices more rapidly break down and do not result in an increase in peak RMS along the centerline. Instead, a slight decrease in the peak centerline RMS is observed (and a slight shift upstream for the $a_0/U_j = 10\%$ forcing). Along the lipline, an increase is observed for $x \in [0, 2]$ corresponding to where the modulation of the $St_f = 1.5$ forcing is dominant.

In Fig. 6, we display the azimuthally averaged Wigner-Ville spectrum of the axial velocity at $x = 1.25,\ 6,\ r = 0.5$, which shows how the PSD of $u_x''$ at these locations varies as a function of the phase of the forcing. These locations were chosen to approximately correspond to the location where the RMS is most phase-dependent for the $St_f = 0.3,\ 1.5$ forcing. The natural jet is known to be statistically stationary, resulting in a power spectrum that is, on average, constant. On the other hand, based on our preceding analysis, it is known that the forcing results in phase-dependent statistics. For the natural jet, we compute the Wigner-Ville spectrum *assuming* a forcing frequency of $St_f = 0.25$ to determine the level of statistical convergence. To compute the spectral estimates, a block length of $N_{fft}$ is used such that $\Delta St \approx 0.05$ for each of the cases. To minimize the variance and reduce cyclic leakage, a phenomenon similar to spectral leakage, an overlap of 67% is used, which is slightly higher than previous studies of natural turbulent jets [12, 19] and that used in SPOD-based data reconstruction [46]. In general, $\alpha_0$ may not equal $St_f$ thus, similar to Heidt and Colonius [20], we scan over all possible values of $\alpha_0$ and confirm that the fundamental cycle frequency present is indeed the forcing frequency, giving $\alpha_0 = St_f$. We consider cycle frequencies up to $\alpha_{max} = 4.5$, resulting in $k_{max} = 15,\ 3$ for the $St_f = 0.3,\ 1.5$ forcing, respectively.

For both locations, we see that the natural jet has no phase dependency indicating that a sufficient level of statistical convergence has been achieved. We clearly observe the localization of the $St_f = 1.5$ forcing and the more global impact of the $St_f = 0.3$ forcing. The $St_f = 0.3$ forcing is seen to have a substantial impact at both locations, while the $St_f = 1.5$ forcing has a minimal impact at $x = 6,\ r = 0.5$, agreeing to the RMS and mean flow figures shown previously. Looking at the mean axial velocity at $x = 6, r = 0.5$ in Fig. 3 for the $a_0/U_j = 1\%,\ 10\%$ cases, we see that at $\theta_f = 0°$ the $a_0/U_j = 1\%$ forcing case is currently low-velocity and the $a_0/U_j = 10\%$ forcing case is currently high-velocity, showing that the high-velocity regions correspond to the more energetic regions in the Wigner-Ville spectrum. A substantial increase in the amount of energy present at the higher frequencies during these high-energy phases is also seen, which is linked to the modulation of the shear layer and passage of the vortices. This clearly demonstrates the benefit of the cyclostationary framework since we are able to explore the statistical decomposition of phase-dependent turbulent structures.

Overall, it is seen that the $a_0/U_j = 1\%$ cases result in a mild modulation, and a large amplitude is required ($a_0/U_j >> 1\%$) to substantially modulate the statistics. Additionally, except for the $St_f = 0.3,\ a_0/U_j = 10\%$ case, the effect on the statistics was minor.

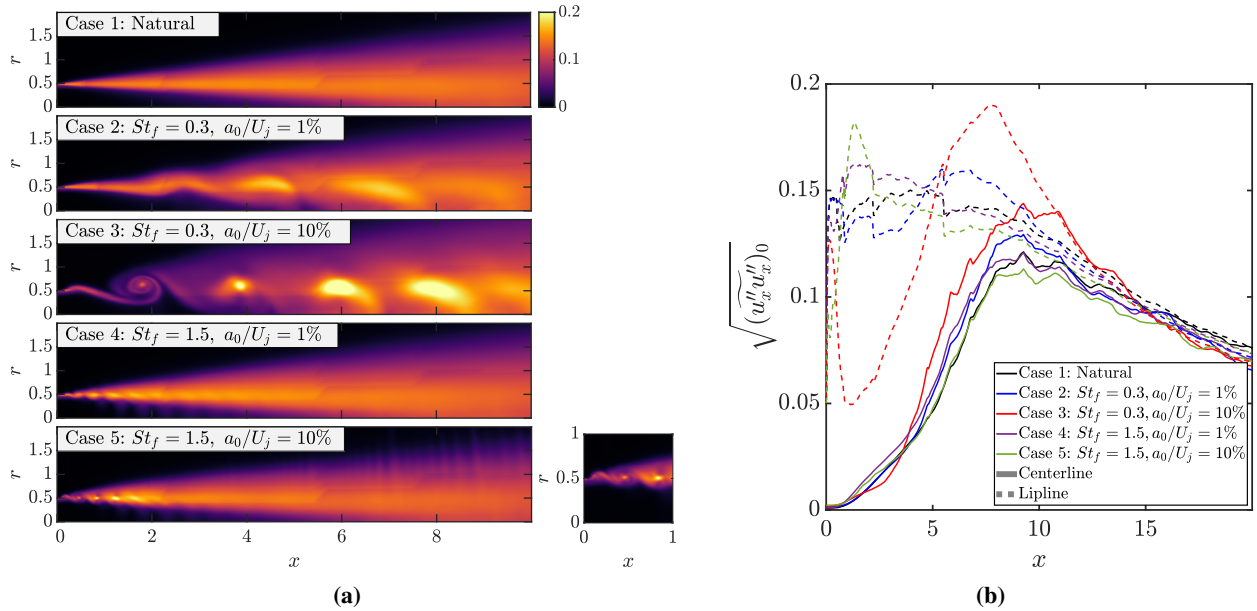


**(a)** **(b)**

**Fig. 5 RMS contours $\sqrt{(\widetilde{u_x''u_x''})}$ at $\theta_f = 0$ (a) and period-averaged RMS $\sqrt{(\widetilde{u_x''u_x''})_0}$ along the centerline and lipline (b) for the subsonic jets.**

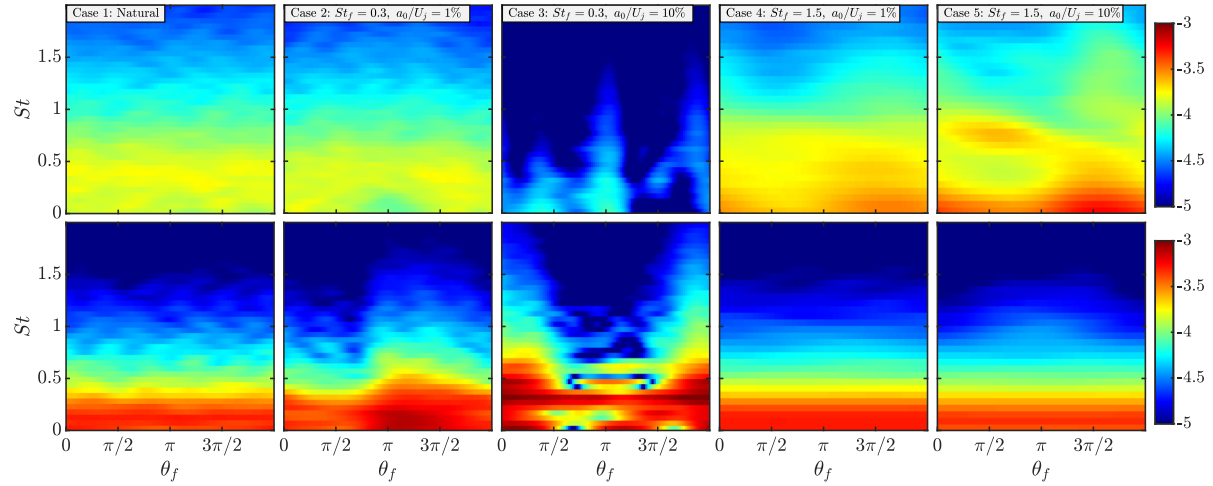


**Fig. 6 Wigner-Ville spectrum of $u_x''$ at $x = 1.5,\ r = 0.5$ (top) and $x = 5,\ r = 0.5$ (bottom) for the subsonic jets, Log10 scale.**

### C. Energy transfer

We now quantify the interaction between the mean field and the turbulent field. To study this, we compute the energy transfer term

$$\widetilde{E}(x, r, \theta, t) = -\overline{\rho}\widetilde{u_i''u_j''}\frac{\partial \widetilde{u}_i}{\partial x_j}, \tag{12}$$

which represents the production of turbulent kinetic energy by the action of the mean field $\widetilde{u}_i$ against the turbulent Reynolds stresses $\widetilde{u_i''u_j''}$. In Fig. 7, we display the azimuthally averaged energy transfer at a phase $\theta_f = 0,\ \pi/3,\ 2\pi/3$, i.e. $\widetilde{E}(x, r, \theta, \theta_f)$. As expected, the $St_f = 0.3$ forcing results in energy transfer towards the end of the potential core, while the $St_f = 1.5$ is localized to $x \in [0,\ 2]$. Similar to the RMS contours, the modulation of the energy transfer for

the $a_0/U_j = 1\%$ forcing cases is relatively minor. For the $a_0/U_j = 10\%$ forcing cases, the modulation is substantial, and the energy transfer from the vortex breakdown is clearly observed.

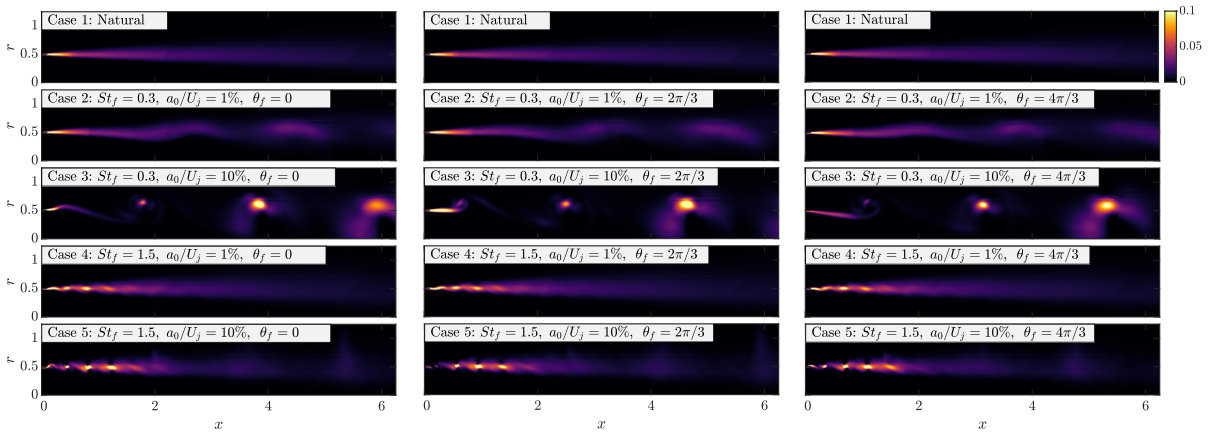


**Fig. 7 Energy transfer contours $\widetilde{E}(x, r, \theta, t)$ for the subsonic jets at $\theta_f = 0$ $(a)$, $\theta_f = 2\pi/3$ $(b)$, $\theta_f = 4\pi/3$ $(c)$.**

Next, we seek to determine the global impact that the forcing has on the energy transfer. We define the cumulative energy transfers by integrating in $r$ and $\theta$,

$$\widetilde{E}_r(x,t) = \int_r \int_\theta \widetilde{E}(x,r,\theta,t) r \partial r \partial \theta, \tag{13}$$

and then, additionally, in $x$,

$$\widetilde{E}_{rx}(x,t) = \int_{x'=0}^{x} \int_r \int_\theta \widetilde{E}(x',r,\theta,t) r \partial r \partial \theta \partial x'. \tag{14}$$

In Fig. 8, we display both $\widetilde{E}_r(x,t)$ and $\widetilde{E}_{rx}(x,t)$. Note that for the natural jet, the vertical lines occurring at $x \approx 0.6,\ 2.2,\ 5.5$ are artifacts of transitions in the LES grid resolution. For the $St_f = 0.3$ cases, at $x \in [0, 10]$, we clearly observe a strong phase-dependent energy transfer. We also observe the axial width and magnitude of the phase-dependent high-energy transfer region increase and then decrease as the degree of mean flow and mean RMS modulation increases and then decreases further downstream. For the $St_f = 1.5$ cases, a similar phenomenon occurs but is spatially restricted to the first 2 diameters downstream, in line with our mean flow observations. After this, another phase-dependent energy transfer phenomenon occurs with a spatial length of $\approx 1.66$, which is exactly the distance that the $St_f = 1.5$ acoustic waves travel in a quiescent media over one forcing cycle. This is linked to a direct nonlinear interaction between the forced acoustic waves and the natural perturbations present in the jet on the outer regions of the jet (where minimal shear is present, resulting in unit phase speed).

Now looking at $\widetilde{E}_{rx}(x,t)$, we see that despite the strong local modulation of energy transfer, the integrated energy transfer is remarkably similar for all cases. Only the strongest forcing ($St_f = 0.3,\ a_0/U_j = 10\%$) results in modest phase-dependence of the energy transfer. In Fig. 9, we display for $\widetilde{E}_{rx}(x,t)$ both the period-averaged minimum and maximum values over the period. We see a similar result, in that only the 10% forcing results in any appreciable modulation in the total energy transfer, with the 1% forcing cases exhibiting minimal phase dependency. Even with the 10% forcing, the variation as a function of phase is minor after a region extending to about $x \approx 1$ for $St_f = 1.5$ and $x \approx 5$ for $St_f = 0.3$.

These results imply that at a given phase, the higher energy transfer linked to the high-velocity regions is mostly canceled out by the lower energy transfer linked to the low-velocity regions. We also observe that after $x = 2,\ 0.7$ for the $St_f = 0.3,\ 1.5$ forcing, the change in the period-averaged energy transfer for the forced jets is large in comparison to the maximum variation as a function of the phase of the forcing. This supports the hypothesis that the primary change in turbulence is driven by a corresponding change to the period-averaged mean, agreeing with previous literature [2, 3]. Furthermore, we note that the impact of the 10% forcing is not an order of magnitude greater than the impact of the 1% forcing (except in the near-nozzle region). This is due to nonlinear interaction inhibiting the growth rate of

the 10% wave, thereby resulting in a reduced impact on the mean field and energy transfer. This demonstrates that a naive increase in the forcing amplitude is not substantially beneficial in modifying the mean/turbulence of a turbulent jet, especially when contending with tonal actuator noise that has reduced the effectiveness of active control devices [2, 3, 45].

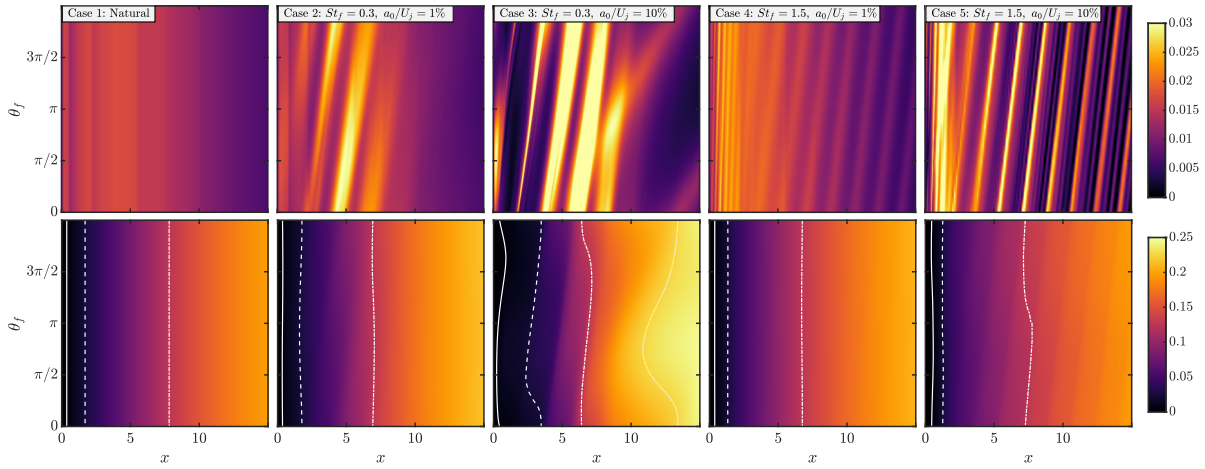


**Fig. 8 Contours of $\widetilde{E}_r(x,t)$ (top) and $\widetilde{E}_{rx}(x,t)$ (bottom) as a function of the phase of the forcing $\theta_f$ and axial location $x$ for the subsonic jets. The white lines overlaid on the $\widetilde{E}_{rx}(x,t)$ contours represent lines of [2, 10, 50, 90]% $\times$ 0.25 energy transfer.**

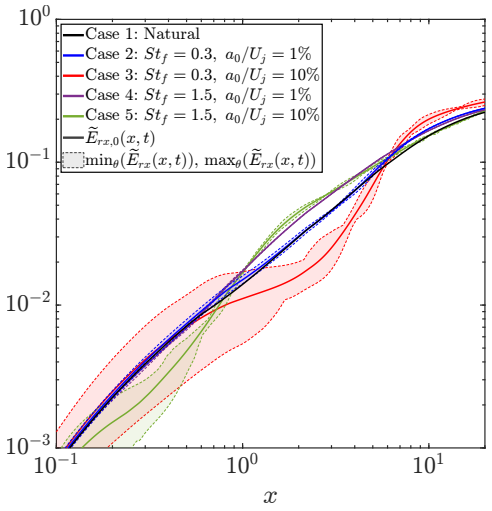


**Fig. 9 Comparison of $\widetilde{E}_{rx,0}(x,t)$ and the maximum fluctuation of $\widetilde{E}_{rx}(x,t)$ for the subsonic jets.**

### D. CS-SPOD

Lastly, we explore the evolution of the coherent structures in the turbulent (non-phase-locked) response of these forced jets. While the preceding analysis has indicated that changes to the turbulence are minor, alteration of the coherent structures could have an outsized impact on the radiated acoustic field [47]. This means that a reduction in the strength of these structures, even if the rest of the turbulence is relativity unimpeded (or even amplified), could lead to substantial reductions in jet noise.

Similar to the computation of the Wigner-Ville spectrum, for each case, we employ a block length of $N_{fft}$ such that $\Delta St \approx 0.025$, an overlap of 67%, and we set $a_2$ such that $f_{max} = 4.5$, where $f_{max}$ is the maximum frequency that CS-SPOD captures (i.e. the maximum frequency in $\Omega_\gamma$). Due to the cyclostationary nature of the forced jets, the

comparison between different forcing frequencies is more difficult. Each CS-SPOD mode contains the set of frequencies $\Omega_\gamma = \{ \cdots, \gamma - 2\alpha_0, \gamma - \alpha_0, \gamma, \gamma + \alpha_0, \gamma + 2\alpha_0, \cdots \}$, and thus, when the forcing frequency changes (i.e. $\alpha_0$ changes), the frequencies contained within $\Omega_\gamma$ also change. This makes a direct frequency-by-frequency comparison, as often performed when using SPOD, impossible. Thus, to keep the analysis between the natural and forced jets as direct as possible, we also compute CS-SPOD of the natural jets, by *assuming* a forcing frequency. One way to think of this is as the limit of forcing at a particular frequency as the amplitude of forcing approaches zero. Theoretically, CS-SPOD modes performed on statistically stationary data (i.e. the natural jet) are identical to SPOD modes where CS-SPOD ranks the energy of all modes computed over the frequency set $\Omega_\gamma$. However, this is not true numerically due to imperfect statistical convergence.

We first investigate the statistical convergence of CS-SPOD. Thus, we compute CS-SPOD on the natural jet with an assumed forcing frequency of $St_f = 0.3,\ 1.5$ as well as regular SPOD. For the natural jet, since SPOD and CS-SPOD are theoretically identical for a statistically stationary flow, we would expect that the CS-SPOD modes contain just a single frequency component at a frequency equal to the component in $\Omega_\gamma$ with maximum energy. Since the energy spectrum of a jet is approximately monotonically decaying for increasing $f$, we would expect the frequency maximum energy component in $\Omega_\gamma$ to be $f = \gamma$. For example, for $St_f = 0.3$ and $\gamma = 0.15$, $\Omega_\gamma = [\cdots, -0.75, -0.45, -0.15, 0.15, 0.45, 0.75, \cdots]$, thus, we would expect the mode to be at a frequency of $f = \pm 0.15$. Similarly, for $St_f = 1.5$ and $\gamma = 0.15$, we would expect the mode to again be at $f = \pm 0.15$.

To assess this proposition, in Fig. 10a, we display the eigenspectrum of the dominant mode as a function of $\gamma, f$ for the natural jet computed with CS-SPOD assuming a forcing frequency of $St_f = 0.3,\ 1.5$ and computed using SPOD. Note that only $\gamma = [0, \alpha_0/2]$ is needed since the $m = 0$ data is real, resulting in a symmetric spectrum. Overall, we see good agreement between the CS-SPOD eigenspectrum with the two assumed forcing frequencies and SPOD. The $St_f = 0.3$ assumed forcing frequency results in a larger deviation from the SPOD eigenspectrum than the $St_f = 1.5$ assumed forcing frequency. This is for two reasons. First, more frequency components are linked together for $St_f = 0.3$, increasing the opportunity for statistical noise to influence the results. Second, since the frequency components are separated by $St_f$, they are closer in energy separation for $St_f = 0.3$ than $St_f = 1.5$ and thus have a greater effect on the statistical convergence. This is also seen in Fig. 10b, where we display the pressure component of the dominant CS-SPOD ($\boldsymbol{\phi}_p(\theta_f)$) at $\gamma,\ f = 0.15$ for the same cases. It is seen that the $St_f = 0.3$ assumed forcing frequency CS-SPOD mode is more polluted with spectral content from other frequencies than the $St_f = 1.5$ case. Thus, care should be taken when interpreting these modes to ensure that statistical artifacts are not misinterpreted.

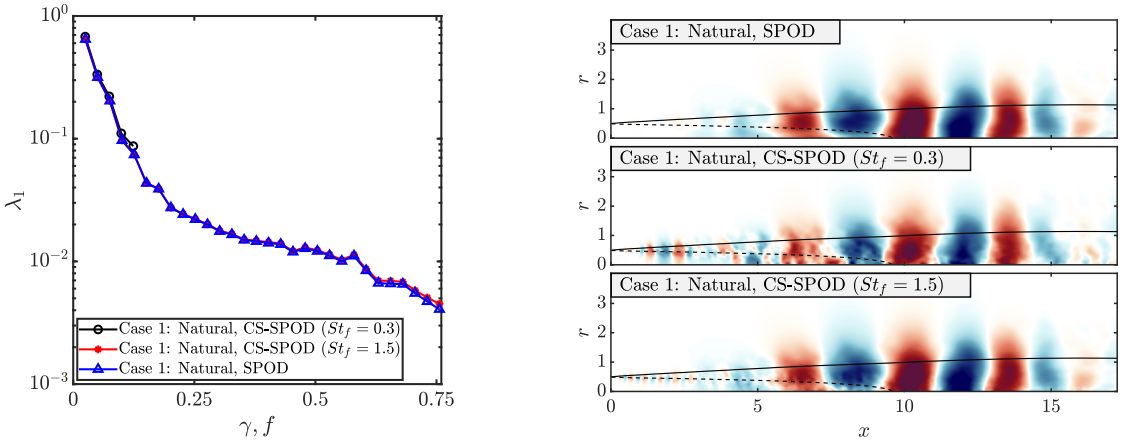


**Fig. 10 Comparison of the dominant mode eigenspectrum (a) and real component of the pressure ($\boldsymbol{\phi_p}(\theta_f = 0)$) at $\gamma, f = 0.15$ at $\theta_f = 0$ (b) of the natural subsonic jet computed using SPOD, CS-SPOD ($St_f = 0.3$), and CS-SPOD ($St_f = 1.5$). Contour limits are given by $\pm 0.75|\boldsymbol{\phi_p}(\theta_f)|_\infty$, where $\boldsymbol{\phi_p}(\theta_f)$ is the current mode being displayed.**

Moving to the results for the forced jets, we first investigate the impact of the $St_f = 0.3$ forcing. In this study, we will focus on the effect of the forcing on the axisymmetric $m = 0$ mode only. In Fig. 11, we display the CS-SPOD

eigenspectrum of the two $St_f = 0.3$ forced jets and the natural jet where a $St_f = 0.3$ has been artificially imposed as discussed above. We observe, for all $\gamma$, an increasing amount of energy in the dominant modes for increasing levels of forcing. In order to determine how the forcing is impacting the generated coherent structures, we display the pressure component of the dominant CS-SPOD mode for the same cases for $\gamma = 0.05,\ 0.15$ in Fig. 12. Since CS-SPOD modes have periodic amplitude in time, in Fig. 12, we display all modes at $\theta = 0$, and then in Fig. 13, we show the temporal evolution of the dominant CS-SPOD for the $St_f = 0.3,\ 10\%$ forced jet at $\gamma = 0.15$. We have also overlaid contours of $\widetilde{u}_x = 0.25,\ 0.75$ to demonstrate how the coherent structures are modulated by the phase-dependent mean velocity.

By looking at the CS-SPOD modes, we note a few salient features. First, all modes are Orr-type modes, which is consistent with the literature for this $m - St$ pair [13], which shows that the dominant mechanism has not changed. Second, we see an upstream shift in the location of the Orr mode corresponding to the change in the time-averaged field. Third, as the forcing amplitude is increased, we observed a strong phase-dependent modulation of the dominant Orr-type mode where the highest-amplitude region of the mode is slaved to the greatest velocity/shear present in the jet. This phase-dependent modulation of the dominant mode is clearly observed in Fig. 13.

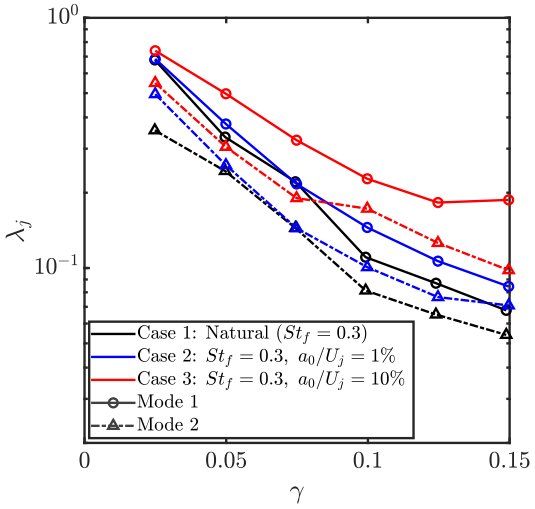


**Fig. 11 Comparison of the CS-SPOD eigenspectrum of the subsonic natural jet and the two forced jets with $St_f = 0.3$.**

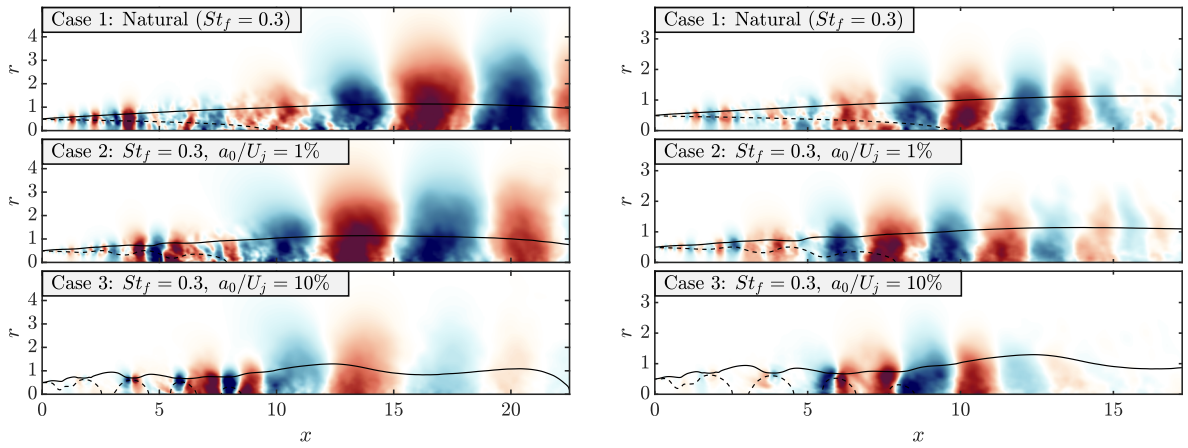


**(a) $\gamma = 0.05$** **(b) $\gamma = 0.15$**

**Fig. 12 Comparison of the real component of pressure component of the dominant mode at $\gamma = 0.05,\ 0.15$ of the natural subsonic jet and the two $St_f = 0.3$ forced jets at $\theta_f = 0$. Contour limits are given by $\pm 0.75|\phi_p(\theta_f = 0)|_\infty$.**

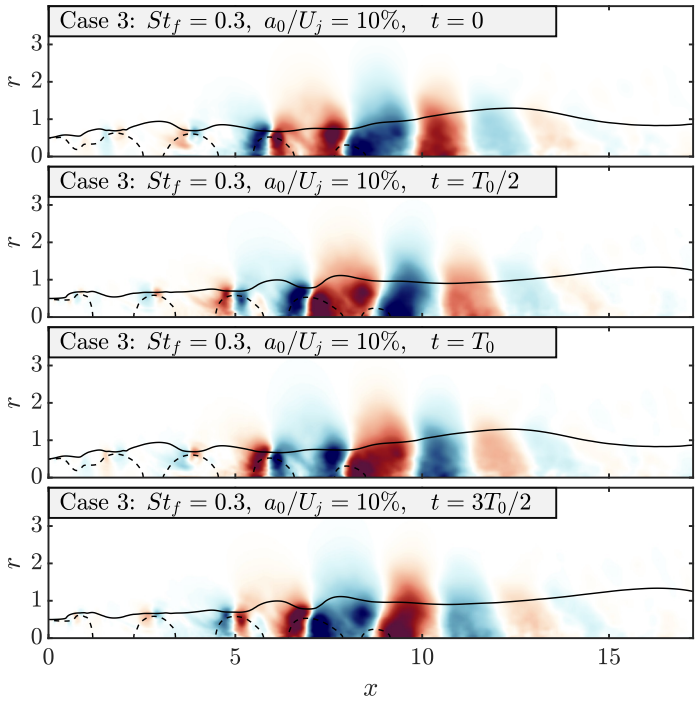


**Fig. 13 Comparison of the real component of pressure component of the dominant mode at $\gamma = 0.15$ of the $St_f = 0.3$, $a_0/U_j = 10\%$ forced subsonic jet at multiple several instances. Contour limits are given by $\pm 0.75|\phi_p(\theta_f = 0)|_\infty$.**

Next, we investigate the impact of the $St_f = 1.5$ forcing. In Fig. 14, we display the CS-SPOD eigenspectrum of the two $St_f = 1.5$ forced jets and the natural jet where a $St_f \approx 1.5$ has been assumed. The spectrum is relatively unaffected by the forcing for approximately $\gamma \in [0, 0.2]$, with a minor decrease in the spectrum for the $a_0/U_j 10\%$ forcing for $\gamma \in [0, 0.05]$. For $\gamma \in [0.2, 0.6]$, we observe a decrease in the eigenspectrum, which continues to decrease for an increased forcing amplitude. Lastly, for approximately $\gamma \in [0.6, 0.75]$, we observe a substantial increase in the energy. Thus, similar to previous studies, our results indicate that high-frequency forcing results in a more stable flow that reduces the amplification of coherent structures. The exception to this is for $\gamma \in [0.6, 0.75]$, where a strong amplification is seen for both forcing amplitudes. A previous study [19] linked this to a direct non-linear phenomenon (i.e. a change in the turbulence that is not attributable to a change in the mean).

In Fig. 15, we display the pressure component of the dominant CS-SPOD mode for the same cases at $\gamma = 0.15,\ 0.475$, and 0.75, which approximately corresponds to the location of no-change, maximum reduction, and maximum amplification seen in the eigenspectrum. We expect that the dominant mechanics at $\gamma = 0.475,\ 0.75$ to be the Kelvin-Helmholtz mechanism [13]. Overall, minor changes to the dominant modes are observed. For $\gamma = 0.15$, the forcing results in a slight increase in the length of the Orr mode. The direct nonlinear interaction between the forcing and naturally coherent structures is described in Secs. V.A and V.C is clearly observed for the $a_0/U_j = 10\%$ forcing. For $\gamma = 0.475$, no substantial change in the mode is observed, while for $\gamma = 0.75$, a reduction in the length of the Kelvin-Helmholtz mode is observed for the forced jet. For $\gamma = 0.15,\ 0.475$, no strong phase-dependent modulation in the dominant modes is observed even for the 10% forcing, while for $\gamma = 0.75$, some phase-dependency is observed for the 10% forcing in the near-nozzle region. This is likely due to the dominant wavelength present in the $\gamma = 0.15,\ 0.475$ modes being much greater than the wavelength of the mean flow deformation caused by the $St_f = 1.5$. This mismatch in the wavelength means that the coherent structures do not react to this modulation and thus evolve independently to this phase-dependent modulation. In contrast, for $\gamma = 0.75$, the primary wavelength is much more similar, resulting in a phase-dependent modulation. Additionally, the spatial support of these longer wavelength structures is much further downstream than the spatial support of the mean flow deformation. Furthermore, Heidt and Colonius [20] showed that when there is a large energy difference at the different frequencies in $\Omega_\gamma$, CS-SPOD can be approximated as SPOD. This is precisely the case for the current case for low $\gamma$, meaning that the modes can be well approximated by their SPOD versions.

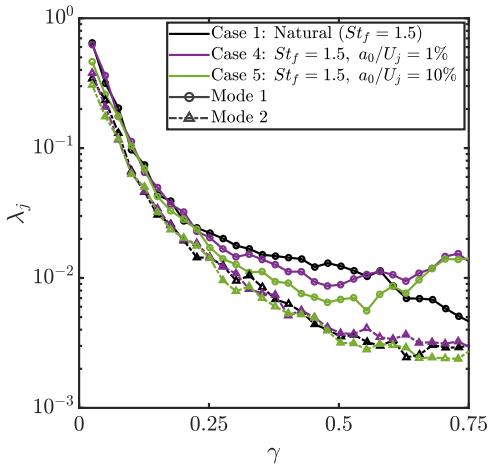


**Fig. 14 Comparison of the CS-SPOD eigenspectrum of the subsonic natural jet and the two forced jets with $St_f = 1.5$.**

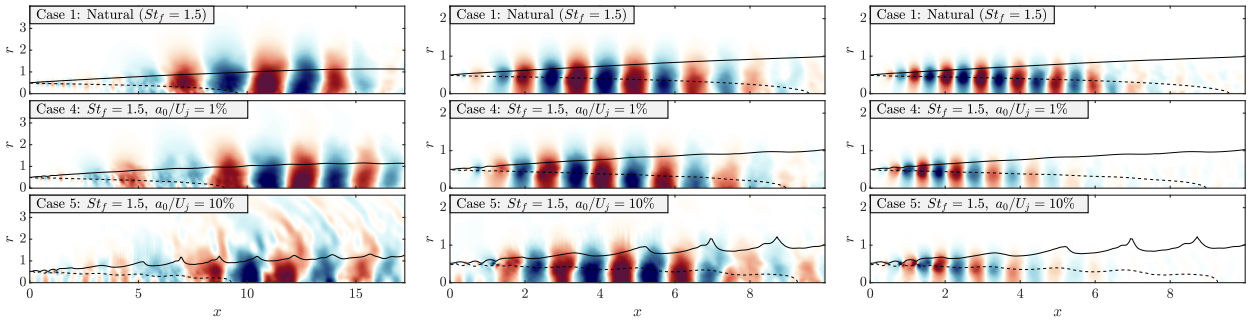


**(a) $\gamma = 0.15$** **(b) $\gamma = 0.475$** **(c) $\gamma = 0.75$**

**Fig. 15 Comparison of the real component of pressure component of the dominant mode at $\gamma = 0.15, 0.475, 0.75$ of the natural subsonic jet and the two $St_f = 1.5$ forced subsonic jets at $\theta_f = 0$. Contour limits are given by $\pm 0.75|\phi_p(\theta_f = 0)|_\infty$.**

## VI. Supersonic jet

To determine the effect of Mach number, we perform a similar analysis on a Mach 1.5 supersonic jet. We have limited our forcing amplitude to 1% to study a realistic forcing amplitude only. In Fig. 16, we display the mean axial velocity corresponding to a forcing phase $\theta_f = 0°$ and the period-averaged axial velocity for the supersonic jets. Visually, we see that the impact of the $St_f = 0.3$ forcing on the centerline mean axial velocity and period-averaged axial velocity is lower for the supersonic jet than the subsonic. Quantitatively, in Fig. 17, the supersonic jet subjected to the $St_f = 0.3$ forcing results in a standard deviation of 10% and 9.5% along the lipline and centerline, respectively. In contrast, the subsonic jet subjected to the same forcing results in a standard deviation of 9.8% and 15%. For the $St_f = 1.5$ forcing, a slight increase in the lipline response is seen with the subsonic and supersonic jets having a standard deviation of 7.0% and 8.5%, respectively. It is also observed that for the supersonic jet, the $St_f = 0.3$ forcing results in a delayed decrease in the centerline velocity and a delayed increase in the momentum thickness, while a rapid decrease in the centerline velocity and rapid increase in the momentum thickness is seen for the $St_f = 1.5$ forcing. This is in contrast to the subsonic jet where the $St_f = 0.3$ forcing resulted in a rapid decrease in the centerline velocity and a delayed increase in the momentum thickness, while the $St_f = 1.5$ forcing resulted in a delayed decrease in the centerline velocity and rapid increase in the momentum thickness.

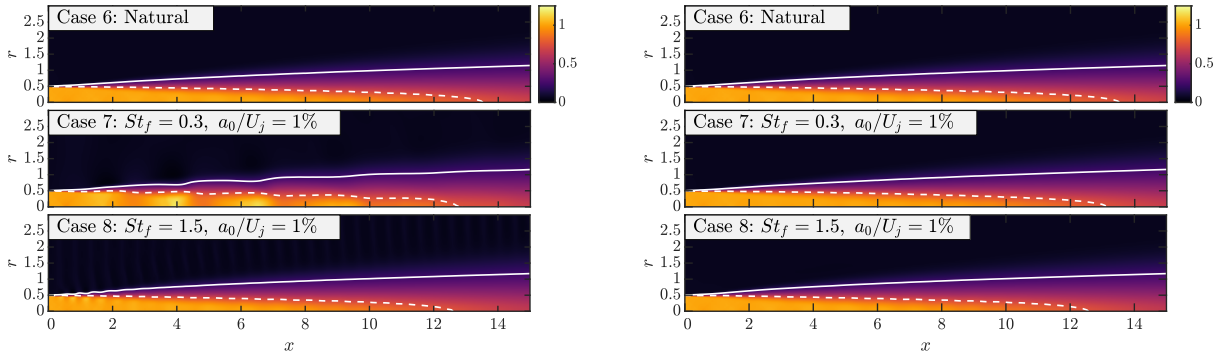


**Fig. 16 Contours of the mean axial velocity $\overline{u}_x$ at $\theta_f = 0$ (a) and the $f = 0$ component (period-averaged component) of the axial velocity $\overline{u}_{x,0}$ (b) for the supersonic jet. The solid and dashed white lines correspond to contours of $\overline{u}_x = 0.25, 0.75$ and $\overline{u}_{x,0} = 0.25, 0.75$ for (a) and (b), respectively.**

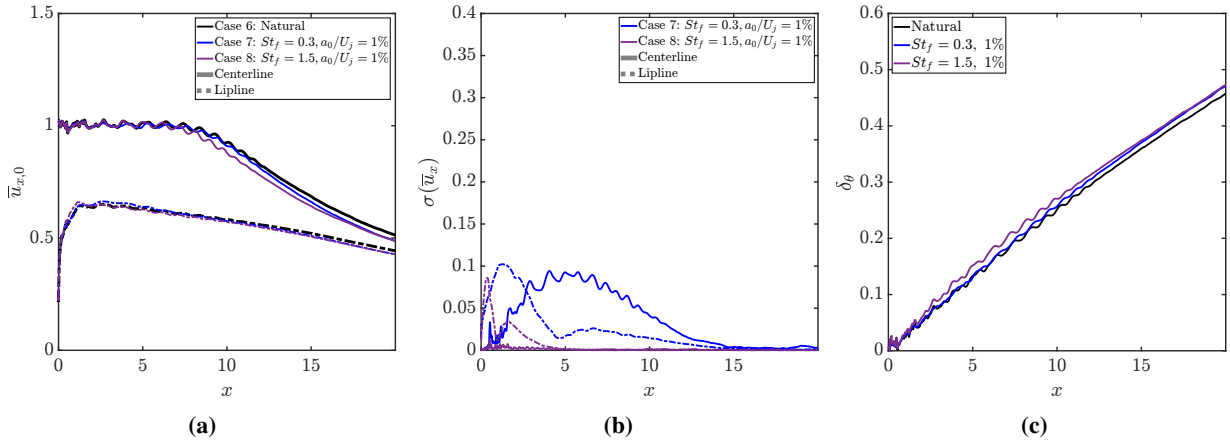


**Fig. 17 Period-averaged axial velocity $\overline{u}_{x,0}$ (a) and standard-deviation of the mean axial velocity $\sigma(\overline{u}_x)$ (b) along the centerline and lipline, and momentum thickness $\delta_\theta$ (c) of the supersonic jet.**

We display the RMS at $\theta_f = 0$ for the supersonic jet in Fig. 18a. We see that the impact on the RMS is similar to the subsonic jet. The $St_f = 0.3$ forcing results in a modulation of the RMS that increases in magnitude until approximately the end of the potential core, while the $St_f = 1.5$ forcing is more localized to the nozzle exit at $x \in [0, 2]$. In Fig. 18b, we see that the $St_f = 0.3$ forcing results in a slight decrease in the period-averaged RMS in the near-nozzle lipline region and a slight increase in the peak RMS towards the end of the potential core. The $St_f = 1.5$ forcing results in a substantial increase in the RMS in the near-nozzle lipline region but a similar peak RMS profile along the centerline that has been shifted upstream by about 1 diameter.

The impact on the energy transfer between the mean flow and turbulence is also similar to that of the subsonic jet, as seen in Figs. 19a and 19b. Like the RMS contours, the greatest modulation of the energy transfer is towards the end of the potential core for the $St_f = 0.3$ forcing and near the nozzle exit for the $St_f = 1.5$ forcing. Similar to the subsonic jet, the $St_f = 0.3$ has minimal effect on the period-averaged integrated energy transfer, while the $St_f = 1.5$ forcing results in a slight increase in period-averaged integrated energy transfer in $x \in [1, 10]$. Furthermore, the maximum modulation of the integrated energy transfer as a function of phase is minimal. This again indicates that any increased regions of energy transfer are canceled out by a corresponding region of reduced energy transfer and that the primary driver of change to the turbulence is a change in the mean field.

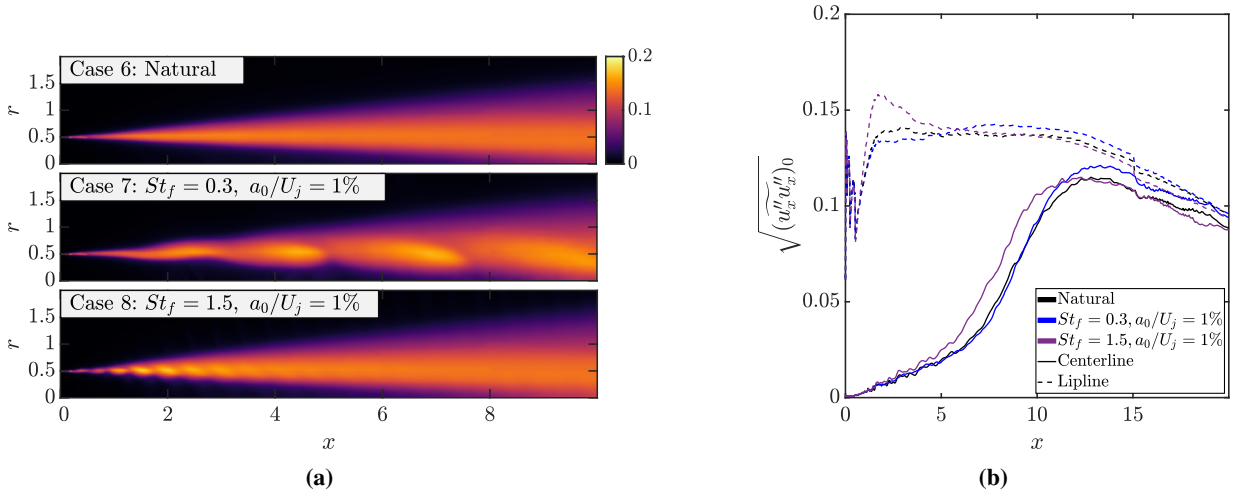


(a) (b)

**Fig. 18 RMS contours $\sqrt{(\widetilde{u_x''u_x''})}$ at $\theta_f = 0$ (a) and period-averaged RMS $\sqrt{(\widetilde{u_x''u_x''})_0}$ along the centerline and lipline (b) for the supersonic jets.**

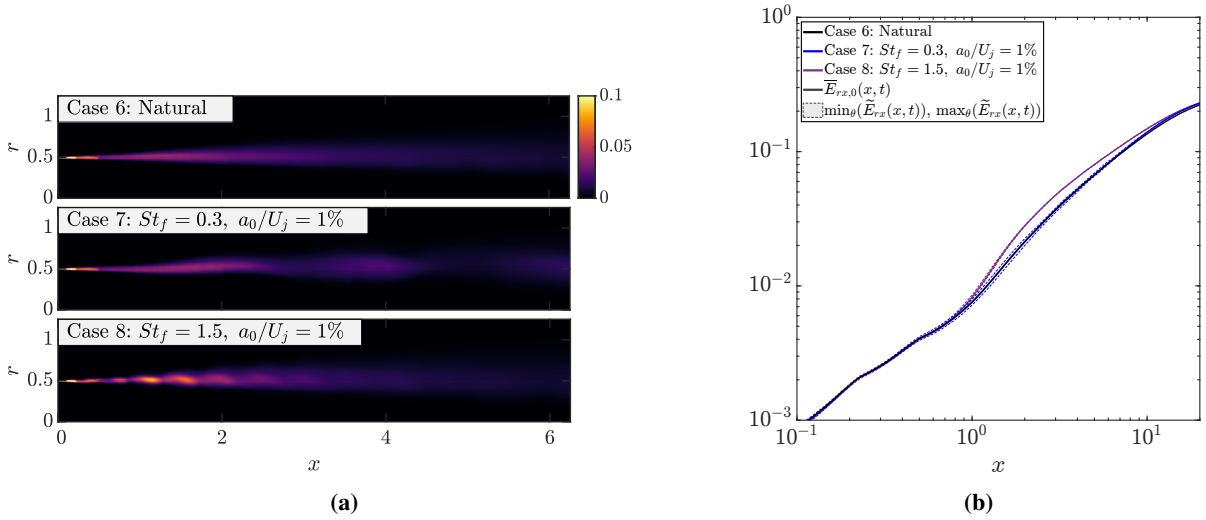


(a) (b)

**Fig. 19 Energy transfer contours $\widetilde{E}(x,r,\theta,t)$ at $\theta_f = 0$ (a) and comparison of $\widetilde{E}_{rx,0}(x,t)$ and the maximum fluctuation of $\widetilde{E}_{rx}(x,t)$ (b) for the supersonic jets.**

Lastly, we investigate the impact of the forcing on the coherent structures present in the supersonic jet using CS-SPOD. In Fig. 20, we display the CS-SPOD eigenspectrum for the forced jets. Both the $St_f = 0.3$ and $St_f = 1.5$ forcing result in a minor change to the spectrum over all values of $\gamma$. Unlike the subsonic jet, no general modification of the spectrum is seen. This is also seen in Fig. 21, where we display the pressure component of the dominant CS-SPOD mode at $\gamma = 0.15$ for the $St_f = 0.3$ forced jet and $\gamma = 0.75$ for the $St_f = 1.5$ forced jet. For the $St_f = 0.3$ forcing, we observe almost no change to the mode, and for $St_f = 1.5$, we observe a contraction in the length of the mode. For $St_f = 1.5$, in the far-field, we can clearly see the direct non-linear interaction between the forcing and the super directivity waves. Overall, it is clear that the differences are smaller for the supersonic jet than the subsonic jet for the $St_f = 0.3$ forcing. In contrast, the $St_f = 1.5$ forcing has a similar impact to the subsonic jet.

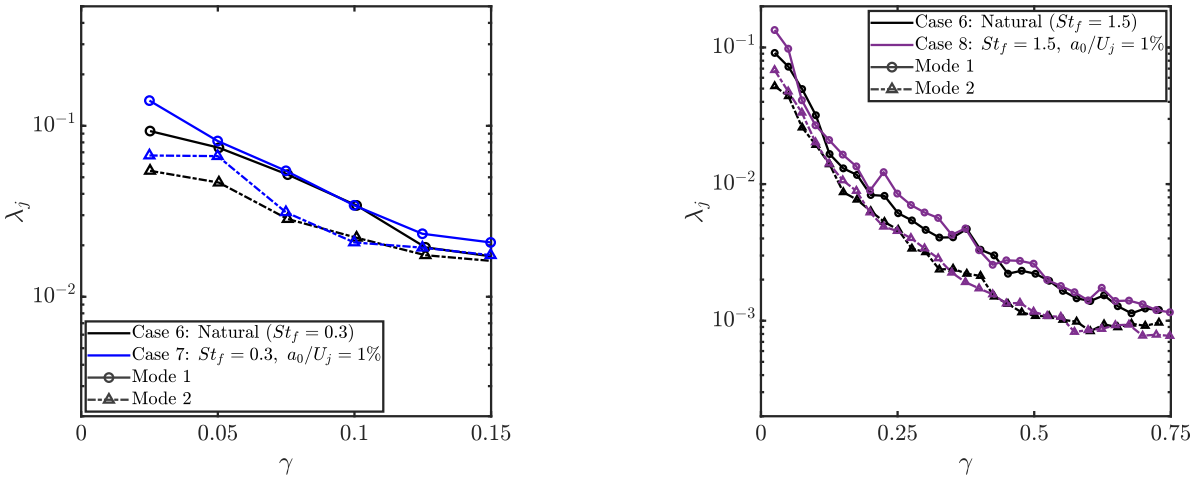


**(a)** **(b)**

**Fig. 20 Comparison of the CS-SPOD eigenspectrum of the supersonic natural jet and the $St_f = 0.3$ (a) and $St_f = 1.5$ (b) forced supersonic jets.**

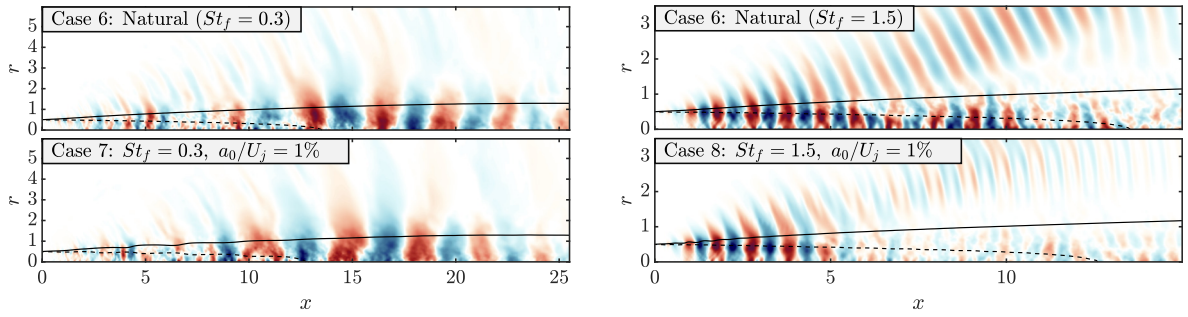


**(a)** **(b)**

**Fig. 21 Comparison of the real component of pressure of the dominant mode at $\gamma = 0.15$ for the natural and $St_f = 0.3$ forced supersonic jets (a) and at $\gamma = 0.75$ for the natural and $St_f = 1.5$ forced supersonic jets. Contour limits are given by $\pm 0.75|\phi_p(\theta_f = 0)|_\infty$.**

## VII. Summary and conclusions

Previous studies [2, 3] have suggested that a periodic forcing is only beneficial to turbulent jet noise reduction to the extent that the forcing results in deformation to the turbulent mean flow. However, a detailed study investigating the mechanisms by which periodic forcing alters the turbulence is lacking. Furthermore, previous investigations have employed a statistically stationary framework that assumes the statistics are invariant in time, thereby neglecting all phase-dependent effects. To fill this gap, we investigated the effect of periodic acoustic forcing by performing a series of large-eddy simulations of turbulent axisymmetric subsonic and supersonic jets subjected to periodic forcing at $St_f = 0.3$, which corresponds to the jet-preferred mode [43], and at $St_f = 1.5$, which corresponds to forcing that previous studies have shown results in a broadband noise reduction [44, 45], at an amplitude of 1%, 10% of the jet velocity. We analyzed the data based on extensions of statistical stationarity to cyclostationarity, i.e. statistics that are periodic in time.

Both the low-frequency $St_f = 0.3$ and high-frequency $St_f = 1.5$ forcing generated an energetic tonal response. The $St_f = 0.3$ forcing exhibited the largest effect towards the end of the potential core while the $St_f = 1.5$ forcing was localized to $x \in [0, 2]$. Despite the strong response, all forcing cases had a limited effect on the period-averaged mean, and a forcing amplitude greater than 1% was required to achieve a small change. The phase-dependency of the statistics was found to follow a similar, but more subtle, trend. The RMS, Wigner-Ville spectrum, and energy transfer between the mean and turbulent fields were found to be mildly modulated by forcing, with only a substantial

modification coming from the $St_f = 0.3,\ a_0/U_j = 10\%$ forcing case. Despite the modulation of the phase-dependent energy transfer, the domain-integrated energy transfer was found to be surprisingly constant as a function of phase, indicating that regions of locally greater energy transfer are canceled out by corresponding region of locally lower energy transfer. Furthermore, the change in the period-averaged energy transfer was found to be substantially larger than the phase-dependent modulation, in contrast to the mean flow modulation where the phase-dependent modulation is much greater. This suggests that the impact of the forcing on the turbulence is minor and that any substantial change to the turbulence needs to be driven by a corresponding change to the period-averaged mean.

We next employed cyclostationary spectral proper orthogonal decomposition (CS-SPOD) to investigate how the dominant coherent structures are modulated by the forcing. For $St_f = 0.3$, a broadband increase in the energy of these structures was found. Furthermore, a phase-dependent modulation of the low-frequency coherent structures was seen, with the high-energy region of the mode being slaved to the high-velocity/high-shear regions of the mean flow. The $St_f = 1.5$ was found to have lower energy over almost the entire spectrum, suggesting that the new period-averaged mean flow is more stable. No phase-dependent modulation of the low-frequency coherent structures was seen due to a large difference in the wavelength and spatial support between the coherent structures and the mean field. Over a small range of $\gamma$, the $St_f = 1.5$ forcing was found to result in a substantial increase in the energy, which a previous study [19] had linked to vortex pairing. However, further investigation is required to prove this. A similar investigation on a $M_j = 1.5$ supersonic jet showed a similar impact of the forcing for the $St_f = 1.5$ forcing and a reduced impact for the $St_f = 0.3$ forcing.

Our results largely confirm conclusions drawn from two earlier studies [2, 3], namely that while the jet is strongly receptive to unsteady forcing, it produces a phase-locked response that has only a modest impact on the period-averaged mean flow and that does not result in any significant reorganization of the turbulence unless the forcing amplitude is substantially high (on the order of 10% of the jet velocity for the present study). Future work includes determining effective forcing strategies based principally on optimizing the deformation of the mean flow field while minimizing the directly radiating component.



## Acknowledgments

The authors gratefully acknowledge support from the United States Office of Naval Research under contract N00014-20-1-2311 with Dr. S. Martens as program manager and the Federal Aviation Administration under grant 13-C-AJFE-UI. This work was supported in part by high-performance computer time and resources from the DoD High Performance Computing Modernization Program. This work used Stampede2 at Texas Advanced Computing Center through allocation CTS120005 from the Advanced Cyberinfrastructure Coordination Ecosystem: Services & Support (ACCESS) program, which is supported by National Science Foundation grants #2138259, #2138286, #2138307, #2137603, and #2138296.

## References

[1] Casalino, D., Diozzi, F., Sannino, R., and Paonessa, A., "Aircraft noise reduction technologies: a bibliographic review," *Aerospace Science and Technology*, Vol. 12, No. 1, 2008, pp. 1–17.

[2] Kœnig, M., Sasaki, K., Cavalieri, A. V., Jordan, P., and Gervais, Y., "Jet-noise control by fluidic injection from a rotating plug: linear and nonlinear sound-source mechanisms," *Journal of Fluid Mechanics*, Vol. 788, 2016, pp. 358–380.

[3] Sinha, A., Towne, A., Colonius, T., Schlinker, R. H., Reba, R., Simonich, J. C., and Shannon, D. W., "Active control of noise from hot supersonic jets," *AIAA Journal*, Vol. 56, No. 3, 2018, pp. 933–948.

[4] Hurd, H., "An Investigation of Periodically Correlated Stochastic Processes, Ph.D. Dissertation," Tech. rep., Duke University, Durham, North Carolina., 1969.

[5] Gardner, W. A., "Representation and estimation of cyclostationary processes," Tech. rep., Massachusetts Univ Amherst Engineering Research Inst, 1972.

[6] Boyles, R., and Gardner, W., "Cycloergodic properties of discrete-parameter nonstationary stochastic processes," *IEEE Transactions on information theory*, Vol. 29, No. 1, 1983, pp. 105–114.

[7] Gardner, W. A., "Introduction to random processes with applications to signals and systems((Book))," *New York, MacMillan Co., 1986, 447*, 1986.

[8] Brown III, W. A., *On the theory of cyclostationary signals*, University of California, Davis, 1987.

[9] Gardner, W. A., "The spectral correlation theory of cyclostationary time-series," *Signal processing*, Vol. 11, No. 1, 1986, pp. 13–36.

[10] Lumley, J. L., "The structure of inhomogeneous turbulent flows," *Atmospheric turbulence and radio wave propagation*, 1967.

[11] Lumley, J. L., *Stochastic tools in turbulence*, Courier Corporation, 2007.

[12] Towne, A., Schmidt, O. T., and Colonius, T., "Spectral proper orthogonal decomposition and its relationship to dynamic mode decomposition and resolvent analysis," *Journal of Fluid Mechanics*, Vol. 847, 2018, pp. 821–867.

[13] Pickering, E., Rigas, G., Nogueira, P. A. S., Cavalieri, A. V. G., Schmidt, O. T., and Colonius, T., "Lift-up, Kelvin–Helmholtz and Orr mechanisms in turbulent jets," *Journal of Fluid Mechanics*, Vol. 896, 2020, p. A2. https://doi.org/10.1017/jfm.2020.301.

[14] Schmidt, O. T., and Towne, A., "An efficient streaming algorithm for spectral proper orthogonal decomposition," *Computer Physics Communications*, Vol. 237, 2019, pp. 98–109.

[15] Cavalieri, A. V., Jordan, P., and Lesshafft, L., "Wave-packet models for jet dynamics and sound radiation," *Applied Mechanics Reviews*, Vol. 71, No. 2, 2019.

[16] Nogueira, P. A., Cavalieri, A. V., Jordan, P., and Jaunet, V., "Large-scale streaky structures in turbulent jets," *Journal of Fluid Mechanics*, Vol. 873, 2019, pp. 211–237.

[17] Nekkanti, A., and Schmidt, O. T., "Modal analysis of acoustic directivity in turbulent jets," *AIAA Journal*, Vol. 59, No. 1, 2021, pp. 228–239.

[18] Kaplan, O., Jordan, P., Cavalieri, A. V., and Brès, G. A., "Nozzle dynamics and wavepackets in turbulent jets," *Journal of Fluid Mechanics*, Vol. 923, 2021, p. A22.

[19] Heidt, L., Colonius, T., Nekkanti, A., Schmdit, O., Maia, I., and Jordan, P., "Analysis of forced subsonic jets using spectral proper orthogonal decomposition and resolvent analysis," *AIAA Aviation 2021 Forum*, 2021, p. 2108.

[20] Heidt, L., and Colonius, T., "Spectral proper orthogonal decomposition of harmonically forced turbulent flows," *arXiv preprint*, 2023.

[21] Kim, K.-Y., North, G. R., and Huang, J., "EOFs of one-dimensional cyclostationary time series: Computations, examples, and stochastic modeling," *Journal of Atmospheric Sciences*, Vol. 53, No. 7, 1996, pp. 1007–1017.

[22] Gardner, W. A., Napolitano, A., and Paura, L., "Cyclostationarity: Half a century of research," *Signal processing*, Vol. 86, No. 4, 2006, pp. 639–697.

[23] Napolitano, A., *Cyclostationary processes and time series: theory, applications, and generalizations*, Academic Press, 2019.

[24] Antoni, J., Bonnardot, F., Raad, A., and El Badaoui, M., "Cyclostationary modelling of rotating machine vibration signals," *Mechanical systems and signal processing*, Vol. 18, No. 6, 2004, pp. 1285–1314.

[25] Antoni, J., "Cyclostationarity by examples," *Mechanical Systems and Signal Processing*, Vol. 23, No. 4, 2009, pp. 987–1036.

[26] Hussain, A. K. M. F., and Reynolds, W. C., "The mechanics of an organized wave in turbulent shear flow," *Journal of Fluid Mechanics*, Vol. 41, No. 2, 1970, pp. 241–258.

[27] Hussain, A., and Reynolds, W., "The mechanics of an organized wave in turbulent shear flow. Part 2. Experimental results," *Journal of Fluid Mechanics*, Vol. 54, No. 2, 1972, pp. 241–261.

[28] Martin, W., "Time-frequency analysis of random signals," *ICASSP'82. IEEE International Conference on Acoustics, Speech, and Signal Processing*, Vol. 7, IEEE, 1982, pp. 1325–1328.

[29] Martin, W., and Flandrin, P., "Wigner-Ville spectral analysis of nonstationary processes," *IEEE Transactions on Acoustics, Speech, and Signal Processing*, Vol. 33, No. 6, 1985, pp. 1461–1470.

[30] Antoni, J., "Cyclic spectral analysis in practice," *Mechanical Systems and Signal Processing*, Vol. 21, No. 2, 2007, pp. 597–630.

[31] Welch, P., "The use of fast Fourier transform for the estimation of power spectra: a method based on time averaging over short, modified periodograms," *IEEE Transactions on audio and electroacoustics*, Vol. 15, No. 2, 1967, pp. 70–73.

[32] Chu, B.-T., "On the energy transfer to small disturbances in fluid flow (Part I)," *Acta Mechanica*, Vol. 1, No. 3, 1965, pp. 215–234.

[33] Schmidt, O. T., Towne, A., Rigas, G., Colonius, T., and Brès, G. A., "Spectral analysis of jet turbulence," *Journal of Fluid Mechanics*, Vol. 855, 2018, pp. 953–982.

[34] Sirovich, L., "Turbulence and the dynamics of coherent structures. I. Coherent structures," *Quarterly of applied mathematics*, Vol. 45, No. 3, 1987, pp. 561–571.

[35] Huang, P., Coleman, G., and Bradshaw, P., "Compressible turbulent channel flows: DNS results and modelling," *Journal of Fluid Mechanics*, Vol. 305, 1995, pp. 185–218.

[36] Reynolds, W., and Hussain, A., "The mechanics of an organized wave in turbulent shear flow. Part 3. Theoretical models and comparisons with experiments," *Journal of Fluid Mechanics*, Vol. 54, No. 2, 1972, pp. 263–288.

[37] Brès, G. A., Ham, F. E., Nichols, J. W., and Lele, S. K., "Unstructured large-eddy simulations of supersonic jets," *AIAA journal*, Vol. 55, No. 4, 2017, pp. 1164–1184.

[38] Brès, G. A., Jordan, P., Jaunet, V., Le Rallic, M., Cavalieri, A. V., Towne, A., Lele, S. K., Colonius, T., and Schmidt, O. T., "Importance of the nozzle-exit boundary-layer state in subsonic turbulent jets," *Journal of Fluid Mechanics*, Vol. 851, 2018, pp. 83–124.

[39] Nekkanti, A., Maia, I., Jordan, P., Heidt, L., Colonius, T., , and Schmidt, O. T., "Triadic nonlinear interactions and acoustics of forced versus unforced turbulent jets," *Twelveth International Symposium on Turbulence and Shear Flow Phenomena (TSFP12)*, Osaka, Japan (Online), July 19-22, 2022.

[40] Maia, I. A., Jordan, P., Cavalieri, A. V. G., Martini, E., and Silvestre, F., "Closed-loop control of forced turbulent jets," *arXiv preprint arXiv:2009.09299*, 2020.

[41] Maia, I. A., Jordan, P., Cavalieri, A. V., Martini, E., Sasaki, K., and Silvestre, F. J., "Real-time reactive control of stochastic disturbances in forced turbulent jets," *Physical Review Fluids*, Vol. 6, No. 12, 2021, p. 123901.

[42] Maia, I. A., Jordan, P., and Cavalieri, A. V., "Wave cancellation in jets with laminar and turbulent boundary layers: The effect of nonlinearity," *Physical Review Fluids*, Vol. 7, No. 3, 2022, p. 033903.

[43] Crow, S. C., and Champagne, F. H., "Orderly structure in jet turbulence," *Journal of Fluid Mechanics*, Vol. 48, No. 3, 1971, p. 547–591. https://doi.org/10.1017/S0022112071001745.

[44] Samimy, M., Kim, J.-H., Kastner, J., Adamovich, I., and Utkin, Y., "Active control of a Mach 0.9 jet for noise mitigation using plasma actuators," *AIAA journal*, Vol. 45, No. 4, 2007, pp. 890–901.

[45] Samimy, M., Kim, J.-H., Kearney-Fischer, M., and Sinha, A., "Acoustic and flow fields of an excited high Reynolds number axisymmetric supersonic jet," *Journal of Fluid Mechanics*, Vol. 656, 2010, pp. 507–529.

[46] Nekkanti, A., and Schmidt, O. T., "Gappy spectral proper orthogonal decomposition," *Journal of Computational Physics*, Vol. 478, 2023, p. 111950.

[47] Jordan, P., and Colonius, T., "Wave packets and turbulent jet noise," *Annual review of fluid mechanics*, Vol. 45, No. 1, 2013, pp. 173–195.